



## RESEARCH ARTICLE

10.1029/2021GC009905

### Key Points:

- Step heating experiments and He diffusion modeling of Fe- and Mn-oxides are consistent with a grain size control on He diffusivity
- Fe- and Mn-oxide (U-Th)/He dates from southeastern Arizona are consistent with Proterozoic-Cenozoic magmatic and tectonic events
- Petrographic and spectroscopic characterizations of Fe- and Mn-oxides help provide context for (U-Th)/He data interpretation

### Supporting Information:

Supporting Information may be found in the online version of this article.

### Correspondence to:

S. H. Scoggin,  
[sscoggi2@uwyo.edu](mailto:sscoggi2@uwyo.edu)

### Citation:

Scoggin, S. H., Reiners, P. W., Shuster, D. L., Davis, G. H., Ward, L. A., Worthington, J. R., et al. (2021). (U-Th)/He and  $^4\text{He}/^3\text{He}$  thermochronology of secondary oxides in faults and fractures: A regional perspective from southeastern Arizona. *Geochemistry, Geophysics, Geosystems*, 22, e2021GC009905. <https://doi.org/10.1029/2021GC009905>

Received 13 MAY 2021

Accepted 19 OCT 2021

# (U-Th)/He and $^4\text{He}/^3\text{He}$ Thermochronology of Secondary Oxides in Faults and Fractures: A Regional Perspective From Southeastern Arizona

Shane H. Scoggin<sup>1,2</sup> , Peter W. Reiners<sup>1</sup>, David L. Shuster<sup>3</sup>, George H. Davis<sup>1</sup>, Lauren A. Ward<sup>1,4</sup> , James R. Worthington<sup>1,5</sup>, Phillip A. Nickerson<sup>1,6</sup>, and Nathan S. Evenson<sup>1,7</sup>

<sup>1</sup>Department of Geosciences, University of Arizona, Tucson, AZ, USA, <sup>2</sup>Now at Department of Geology and Geophysics, University of Wyoming, Laramie, WY, USA, <sup>3</sup>Department of Earth and Planetary Science, University of California, Berkeley, CA, USA, <sup>4</sup>Now at Department of Earth Sciences, University of Hawai'i, Honolulu, HI, USA, <sup>5</sup>Now at Geosciences Research Division, Scripps Institution of Oceanography, University of California San Diego, La Jolla, CA, USA, <sup>6</sup>Now at Rio Tinto Exploration, Salt Lake City, UT, USA, <sup>7</sup>Now at Kane Environmental Inc., Seattle, WA, USA

**Abstract** Fe- and Mn-oxides are common secondary minerals in faults, fractures, and veins and potentially record information about the timing of fluid movement through their host rocks. These phases are difficult to date by most radioisotopic techniques, but relatively high concentrations of U and Th make the (U-Th)/He system a promising approach. We present new petrographic, geochronologic and thermochronologic analyses of secondary oxides and associated minerals from fault zones and fractures in southeastern Arizona. We use these phases in attempt to constrain the timing of fluid flow and their relationship to magmatic, tectonic, or other regional processes. In the shallowly exhumed Galiuro Mountains, Fe-oxide (U-Th)/He dates correspond to host-rock crystallization and magmatic intrusions from ca. 1.6 to 1.1 Ga. Step-heating  $^4\text{He}/^3\text{He}$  experiments and polydomain diffusion modeling of  $^3\text{He}$  release spectra on these samples are consistent with a crystallite size control on He diffusivity, and little fractional loss of radiogenic He since formation in coarse-grained hematite, but large losses from fine-grained Mn-oxide. In contrast to Proterozoic dates, Fe- and Mn-oxides from the Catalina-Rincon and Pinaleno metamorphic core complexes are exclusively Cenozoic, with dates clustering at ca. 24, 15, and 9 Ma, which represent distinct cooling or fluid-flow episodes during punctuated periods of normal faulting. Finally, a subset of Fe-oxides yield dates of ca. 5 Ma to 6 ka and display either pseudomorphic cubic forms consistent with oxidative retrogression of original pyrite or magnetite, or fine-grained botryoidal morphologies that we interpret to represent approximate ages of recrystallization or pseudomorphic replacement at shallow depths.

**Plain Language Summary** (U-Th)/He dating is increasingly applied to secondary Fe- and Mn-oxide minerals in an attempt to understand the timing of fluid-rock reactions associated with magmatic intrusions, fault activity, or other forcings. However, accurate interpretations of secondary oxide thermochronology data requires consideration of potential complications that can lead to multiple interpretations. Here we present (U-Th)/He and  $^4\text{He}/^3\text{He}$  thermochronologic analyses along with chemical and textural observations and provide a geologic context for secondary Fe- and Mn-oxides from southeastern Arizona, in an attempt to better understand how the data relate to geologic processes. Many of these minerals formed and/or cooled in fault zones and fractures at times associated with magmatic or tectonic activity, but some were also recrystallized or pseudomorphically replaced by later fluid-rock reactions. We also provide evidence that He diffusivity is governed by crystal sizes, and that crystal shape and chemical composition should be considered when interpreting (U-Th)/He data of Fe- and Mn-oxides.

## 1. Introduction

### 1.1. Oxide (U-Th)/He Geochronology and Thermochronology

Hematite and other secondary Fe- and Mn-oxides often precipitate in shallow crustal faults and fractures and reflect episodes of fluid-rock reactions (Ault et al., 2015; Calzolari et al., 2018; Evenson et al., 2014; Garcia et al., 2018; Reiners et al., 2014). Several studies have presented geochronologic and thermochronologic dates of secondary oxides that provide constraints on the timing of fluid flow and potentially the timing of faulting and fracturing (Ault et al., 2015, 2016; Calzolari et al., 2018; Evenson et al., 2014; Farley & Flowers, 2012; Farley

© 2021 The Authors.

This is an open access article under the terms of the [Creative Commons Attribution-NonCommercial License](https://creativecommons.org/licenses/by-nc/4.0/), which permits use, distribution and reproduction in any medium, provided the original work is properly cited and is not used for commercial purposes.

& McKeon, 2015; Garcia et al., 2018; Moser et al., 2017). In most cases, these studies are limited to relatively small regions, and in some cases the significance of the dates are subject to multiple interpretations due to the potential for recrystallization, pseudomorphic replacement, and/or open-system behavior (particularly diffusive He loss and post-crystallization U uptake; Ault et al., 2015; Farley & Flowers, 2012; Garcia et al., 2018; Reiners et al., 2014; Wernicke & Lippolt, 1993, 1994). By examining data sets from samples collected over a larger region spanning the depths of Cenozoic exhumation, fault and fracturing histories, and paleo-fluid-flow regimes, we aim to elucidate patterns and explicit clusters of oxide (U-Th)/He dates that may aid interpretation of oxide (U-Th)/He dates in general. Using multiple methods including  $^4\text{He}/^3\text{He}$  thermochronometry, optical and scanning electron microscopy (SEM) including back-scatter electron (BSE) and secondary electron (ESED) microscopy, energy-dispersive X-ray spectroscopy (EDS), and electron probe microanalysis (EPMA) to investigate the significance of (U-Th)/He dates we hope to better contextualize the chemical characteristics of secondary oxides as well as textural clues leading to oxide precipitation, crystallization, and cooling histories and how crystal morphologies are manifest in dates.

Here we present new Fe- and Mn-oxide (U-Th)/He dates of polycrystalline aliquots from fault zones, fractures and quartz/hematite veins across a  $\sim 100$  km SW–NE transect in southeastern Arizona (Figure 1a). The study area comprises several mountain ranges with mid-Cenozoic exhumation times but from variable depths with distinct thermal histories. These ranges include the footwall and hanging wall blocks of deeply exhumed metamorphic core complexes and footwalls of higher-angle and lower-magnitude-slip faults (Davis et al., 2004; Dickinson, 1991). We also present  $^4\text{He}/^3\text{He}$  diffusion experiment results from two polycrystalline Fe-oxide and one Mn-oxide samples that support Proterozoic crystallization ages of these samples and the correspondence of the modeled He diffusion-domain size and the microscopically observable crystallite size distributions. These latter results are important for understanding the diffusive properties of He within oxide crystals and how crystallization and cooling histories may then be interpreted (Farley, 2018; Farley & Flowers, 2012; Farley & McKeon, 2015; Wernicke & Lippolt, 1993, 1994).

Previous  $^4\text{He}/^3\text{He}$  thermochronology studies of single-grain and polycrystalline aggregates of Fe-oxides have calculated a closure temperature range for the system from 250 to 50°C, and have suggested individual crystallites in polycrystalline aggregates represent individual diffusion domains (Evenson et al., 2014; Farley, 2018; Farley & Flowers, 2012; Jensen et al., 2018). Comparatively little work has been completed on the Mn-oxide (U-Th)/He system; however, Lippolt and Hautmann (1995) suggest Mn-oxides are suitable candidate minerals for (U-Th)/He thermochronology by showing  $^4\text{He}$  release spectra from diffusion experiments and (U-Th)/He cooling dates that are younger than, but resemble  $^{40}\text{Ar}/^{39}\text{Ar}$  dates, and reflect closure temperatures  $< 250$  °C. Recent studies including Evenson et al. (2014) have reported reproducible Mn-oxide (and Fe-oxide) (U-Th)/He dates from the Buckskin Mountains in western Arizona. Helium diffusion experiments offer quantitative insights into potential post-formation He loss, thermal histories, and diffusion-domain size distributions that microscopy and (U-Th)/He analyses alone cannot provide.

## 2. Geologic Setting

We characterized and measured (U-Th)/He dates on 18 Fe-oxides and three Mn-oxides from quartz/hematite veins, fault zones, and fractures from a SW–NE transect across three adjacent but topographically distinct ranges: The Catalina-Rincon and Pinaleno-Jackson Mountain metamorphic core complexes, and the Galiuro Mountains (Figure 1a). Sample locations, notes, and morphologies are reported in Table 1.

11 samples are from the southwestern part of the transect in both the hanging wall and footwall of the Catalina-Rincon metamorphic core complex where exhumation from estimated depths of  $\sim 14$  km (e.g., Anderson et al., 1988) was previously dated to ca. 30–20 Ma by Fayon et al. (2000) with apatite and zircon fission-track thermochronology. The Catalina-Rincon core complex is bounded to the east by the San Pedro detachment fault and the Martinez Ranch fault, and to the west by the Catalina detachment fault and Pirate fault (Davis et al., 2004; Dickinson, 1991). The footwall of the Catalina-Rincon core complex comprises intrusions of ca. 1.4 Ga Oracle granite, intrusions of the ca. 70–60 Ma Laramide continental arc, intrusions of the ca. 60–45 Ma Wilderness suite granites, intrusions of the ca. 25 Ma Catalina granite, and upper Paleozoic sediments (Creasey et al., 1977; Davis et al., 2004; Dickinson, 1991; Ducea et al., 2020; Fornash et al., 2013; Keith et al., 1980; Terrien, 2012). The hanging wall consists of Paleozoic to Cenozoic sediments

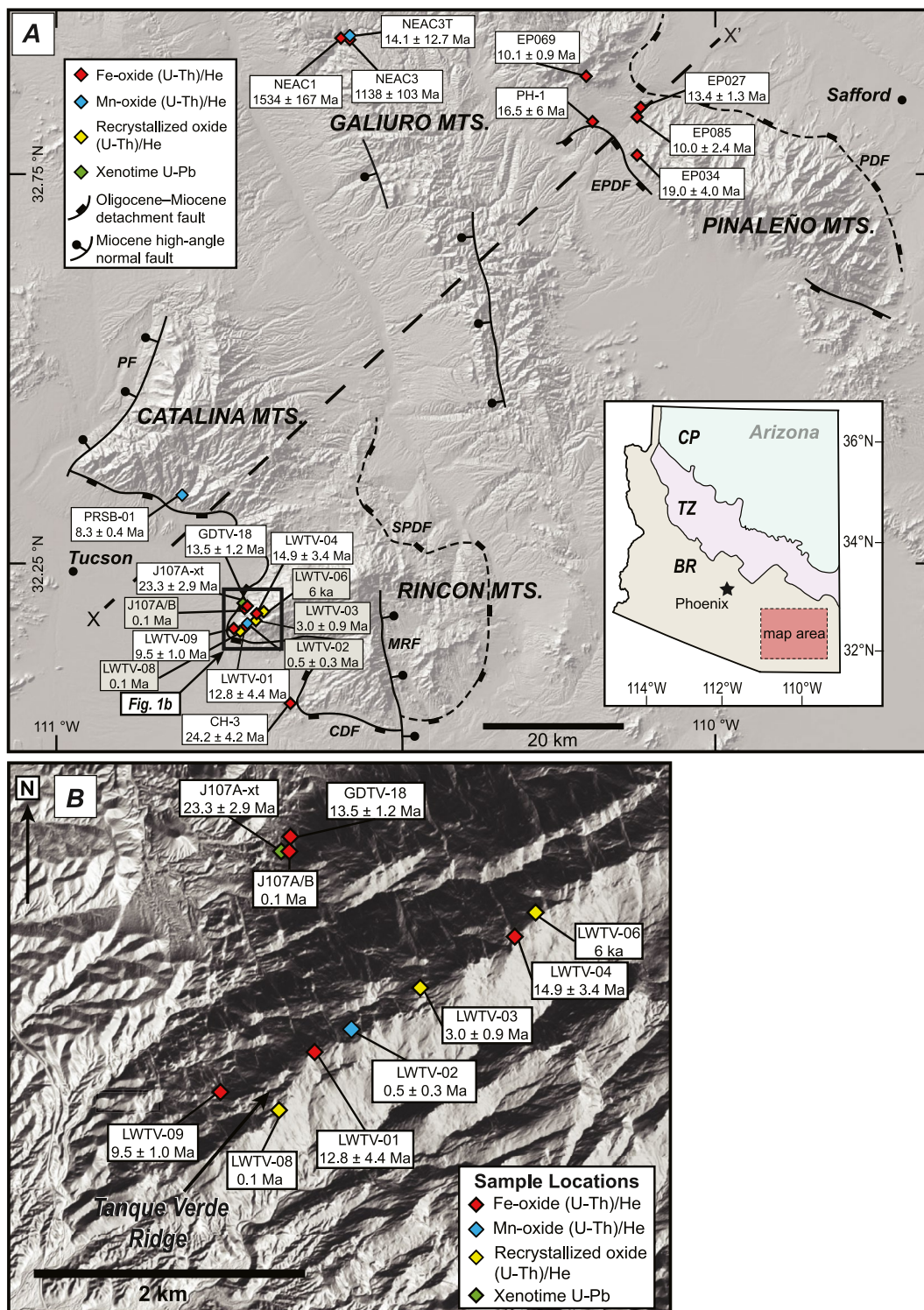


**Figure 1.** (a) Regional map of southeastern Arizona showing Fe- and Mn-oxide (U-Th)/He and xenotime U-Pb dates. Dates are reported as the weighted means of aliquots from that sample. Major fault systems in the region are labeled (PDF = Pinaleno detachment fault, EPDF = Eagle Pass detachment fault, SPDF = San Pedro detachment fault, CDF = Catalina detachment fault, PF = Pirate fault, MRF = Martinez Ranch fault). Fault orientations and locations are from Davis and Hardy (1981), Dickinson (1991), and Thorman and Naruk (1987). Black rectangle in Figure 1a indicates area of Figure 1b. Inset map in Figure 1a shows physiographic provinces of Arizona (CP = Colorado Plateau, TZ = transition zone, BR = Basin and Range). (b) Lidar image of Tanque Verde Ridge. Systematic fractures trend NW-SE perpendicular to the trend of the ridge.

**Table 1**  
*Sample Locations, Notes, Textures, and Dates*

Sample	Latitude °N	Longitude °W	Oxide type	Crystallite morphology	WMD ± 2σ (Ma)
<b>Santa Catalina and Rincon Mountains</b>					
PRSB-01	32.3228	110.8085	Mn-oxide coating on fracture plane	Massive/botryoidal ≤25 μm	8.3 ± 0.4
J107A	32.1740	110.7159	Hematite coating on fracture plane in Catalina detachment fault zone	Botryoids ≤20 μm	0.1 ± 0.02
J107B	32.17340	110.7159	Hematite coating on fracture plane in Catalina detachment fault zone	Botryoids ≤20 μm	0.1 ± 0.3
GDTV-18	32.17340	110.7159	Quartz/hematite veins in Catalina detachment fault zone	Specular blades 10–100 μm	13.5 ± 1.2
CH-3	32.0594	110.6365	Hematite coating on fracture plane in hanging wall	Botryoids 20–75 μm	24.2 ± 4.2
LWTV-01	32.1616	110.7136	Quartz/hematite vein in fault breccia	Specular blades 10–50 μm	12.8 ± 4.4
LWTV-02	32.1632	110.7101	Mn-oxide coating on fracture plane	Massive ≤5 μm	0.5 ± 0.3
LWTV-03	32.1658	110.7061	Quartz/hematite vein in orthogneiss	Cubic pseudomorphs of hematite after pyrite 10–100 μm	3.0 ± 0.9
LWTV-04	32.1694	110.6979	Hematite coating on fracture plane	Specular blades 10–200 μm	14.9 ± 3.4
LWTV-06	32.1709	110.6960	Quartz/hematite vein in mylonite	Cubic pseudomorphs of hematite after magnetite 10–25 μm	0.006 ± 0.003
LWTV-08	32.1573	110.7169	Quartz/hematite vein in mylonite	Cubic pseudomorphs of hematite after pyrite 10–20 μm and specularite ≥10 μm	0.1 ± 0.2
LWTV-09	32.1585	110.7209	Hematite vein in fault breccia	Specular blades 10–50 μm and massive Fe-oxide/oxyhydroxide	9.5 ± 1.0
<b>Pinaleno Mountains – Eagle Pass</b>					
PH-1	32.8005	110.1895	Hematite coating on fracture plane in Eagle Pass detachment fault	Specular blades 5–50 μm	16.5 ± 6.0
EP027	32.1898	110.1119	See Figure S2a–S2d in Supporting Information S1).		13.4 ± 1.3
EP034	32.7495	110.1296			19.0 ± 4.0
EP069	32.8585	110.1969			10.1 ± 0.9
EP085	32.8137	110.1134			10.0 ± 2.4
<b>Galiuro Mountains – Aravaipa Canyon</b>					
NEAC1	32.9102	110.5539	Quartz/hematite vein in Pinal Schist	Specular blades 10–200 μm in quartz matrix	1534 ± 167
NEAC3	32.9127	110.5453	Hematite coating on fracture plane in Pinal Schist	Specular blades 5–150 μm in quartz matrix	1138 ± 103
NEAC3T	32.9127	110.5456	Mn-oxide intergrown with hematite coating on fracture plane in Pinal Schist	Massive ≤5 μm	14.1 ± 12.7

*Note.* Sample names and locations, oxide type, and crystallite size/morphology information along with the WMD (weighted mean date, calculated by adding in quadrature the instrumental uncertainty and standard deviation of the aliquot dates for each sample). Samples with dates <1 Ma were not corrected for U-series disequilibrium.

(Davis et al., 2004; Dickinson, 1991). Evidence for brittle overprinting of ductile deformation is common as fractures and cataclasites over centimeter to meter scales in the footwall, and is common along the southern front of the Catalina Mountains and along Tanque Verde Ridge in the Rincon Mountains, where we hypothesize that the pronounced NW–SE trending lineaments (parallel to the strike of the detachment fault) are dilational fractures associated with late-stage core complex exhumation (Figure 1b). Hematite samples J107A, J107B, and GDTV-18 are from cataclastic fault rocks of suspected Oracle granite (1.4 Ga) origin, Fe-oxide and Mn-oxide samples from Tanque Verde Ridge LWTV-01, LWTV-02, LWTV-03, LWTV-08, and LWTV-09 are from mylonitic Oracle granite and samples LWTV-04 and LWTV-06 are from mylonitic Wilderness suite (ca. 60–45 Ma) granites. Mn-oxide sample PRSB-01 is from fractures in Oracle granite and hematite sample CH-3 is from Cretaceous sediments in the hanging wall of the Catalina detachment fault (Figures 1a and 1b).

We collected six oxide samples from Eagle Pass, the northeast-most area of the transect, in the footwall of the Pinaleno-Jackson Mountain metamorphic core complex where the timing of extension and exhumation from mid-crustal depths have previously been interpreted to be contemporaneous with the Catalina-Rincon core complex ca. 32–19 Ma with hornblende, muscovite, and biotite  $^{40}\text{Ar}/^{39}\text{Ar}$  thermochronology, and ca. 25 Ma with apatite fission-track thermochronology (Jepson et al., 2021; Long et al., 1995). The Pinaleno-Jackson Mountain metamorphic core complex is bounded to the east by the Pinaleno detachment fault, and to the west by the Eagle Pass detachment fault (Davis & Hardy, 1981; Long et al., 1995; Thorman & Naruk, 1987; Figure 1a). The footwall of the Pinaleno-Jackson Mountain core complex comprises intrusions of the ca. 1.6 Ga Johnny Lyon granodiorite, intrusions of ca. 1.4 Ga Oracle granite, and intrusions of ca. 1.1 Ga diabase, and intermediate intrusive dikes emplaced ca. 26 Ma in the Eagle Pass region (Bright et al., 2014; Davis & Hardy, 1981; Long et al., 1995; Nickerson, 2012; Thorman & Naruk, 1987). Rocks in the hanging wall consists of Cenozoic sediments including the ca. 27 Ma Galiuro Volcanics present in the hanging wall of the Eagle Pass detachment fault (Davis & Hardy, 1981; Nickerson, 2012; Shafiqullah et al., 1980). Hematite samples EP027, EP034, and EP085 are from ca. 26 Ma dikes and Proterozoic host rocks (ca. 1.6 Ga) while sample EP069 was taken from a shear zone between two Proterozoic igneous units approximately 10 km NW of the 26 Ma Eagle Pass dikes (Nickerson, 2012). Sample PH-1 was taken from cataclastic fault rocks of suspected 1.6 Ga age.

We also sampled three oxides exposed in Proterozoic basement rocks in the northern Galiuro Mountains. Proterozoic basement exposures of the northern Galiuro Mountains include 1.7–1.6 Ga Pinal “Schist” a regionally diverse subduction/arc complex of the Mazatzal Orogeny in the southwestern U.S. (which is predominantly felsic metavolcanic rocks in this region, opposed to metapelitic lithologies exposed to the west of the Galiuro Mountains) (Bickford et al., 2019; Condie & DeMalas, 1985; Copeland & Condie, 1986; Eisele & Isachsen, 2001; Keep, 1996; Meijer, 2014) and ca. 1.1 Ga diabase intrusions (Bright et al., 2014; Krieger, 1968). The Galiuro Mountains are a NW–SE trending range flanked by mid-Cenozoic normal faults related to the same extensional episode responsible for the exhumation of core complexes to the northeast and southwest (Creasey & Krieger, 1978; Davis & Hardy, 1981; Dickinson, 1991). In contrast to the core complexes, however, the Galiuro Mountains do not expose ductility-deformed mid-crustal rocks and are instead dominated by several kilometers of stratigraphic section of shallow volcanic and volcanoclastic units deposited during regional hyperextension at ca. 27 Ma (Arca et al., 2010; Creasey & Krieger, 1978; Dickinson, 1991; Favorito & Seedorff, 2018; Krieger, 1968). Samples NEAC1, NEAC3, and NEAC3T, from 1.7 to 1.6 Ga rhyolite of Pinal “Schist,” include one Fe-oxide from a quartz/hematite vein and one Fe-oxide co-occurring with Mn-oxide from a fracture plane.

### 3. Sample Descriptions

#### 3.1. Santa Catalina and Rincon Mountains

##### 3.1.1. Recrystallized/Metasomatized Oxides From Tanque Verde Ridge

Three Fe-oxide samples from the footwall of the Catalina detachment fault on Tanque Verde Ridge display recrystallization or pseudomorphic replacement textures of hematite after pyrite or magnetite. Sample LWTV-03 is a hematite sample from a quartz/hematite vein found in a quartz-rich gneiss (Figure 2a). Abundant cubic pseudomorphs of hematite after pyrite are present with widths ranging from 10 to 100  $\mu\text{m}$ . Subtle shading differences in BSE indicate variable Fe contents throughout the cubes. EDS analyses show trace amounts of S, as well as Al and Si in and surrounding cubes. Sample LWTV-06 is a hematite coating on mylonitic gneiss with slickenlines and abundant cubic pseudomorphs of hematite possibly after magnetite as no sulfur was found in microprobe and EDS analyses (Figure 2b). Cubes range in size from 10 to 25  $\mu\text{m}$  across and contain dispersed concentrations of Mn, Ti, and Na. Sample LWTV-08 is hematite from a quartz-vein found in mylonite and exhibits a combination of both specularite blades and relict cubic pseudomorphs of hematite possibly after pyrite toward the edges of the vein (Figure 2c). EDS and EPMA analyses reveal minor S concentrations throughout the cubes. Cubes from this sample range approximately 10–20  $\mu\text{m}$  across, while hematite blades are 5–10  $\mu\text{m}$  across and 10–50  $\mu\text{m}$  long.

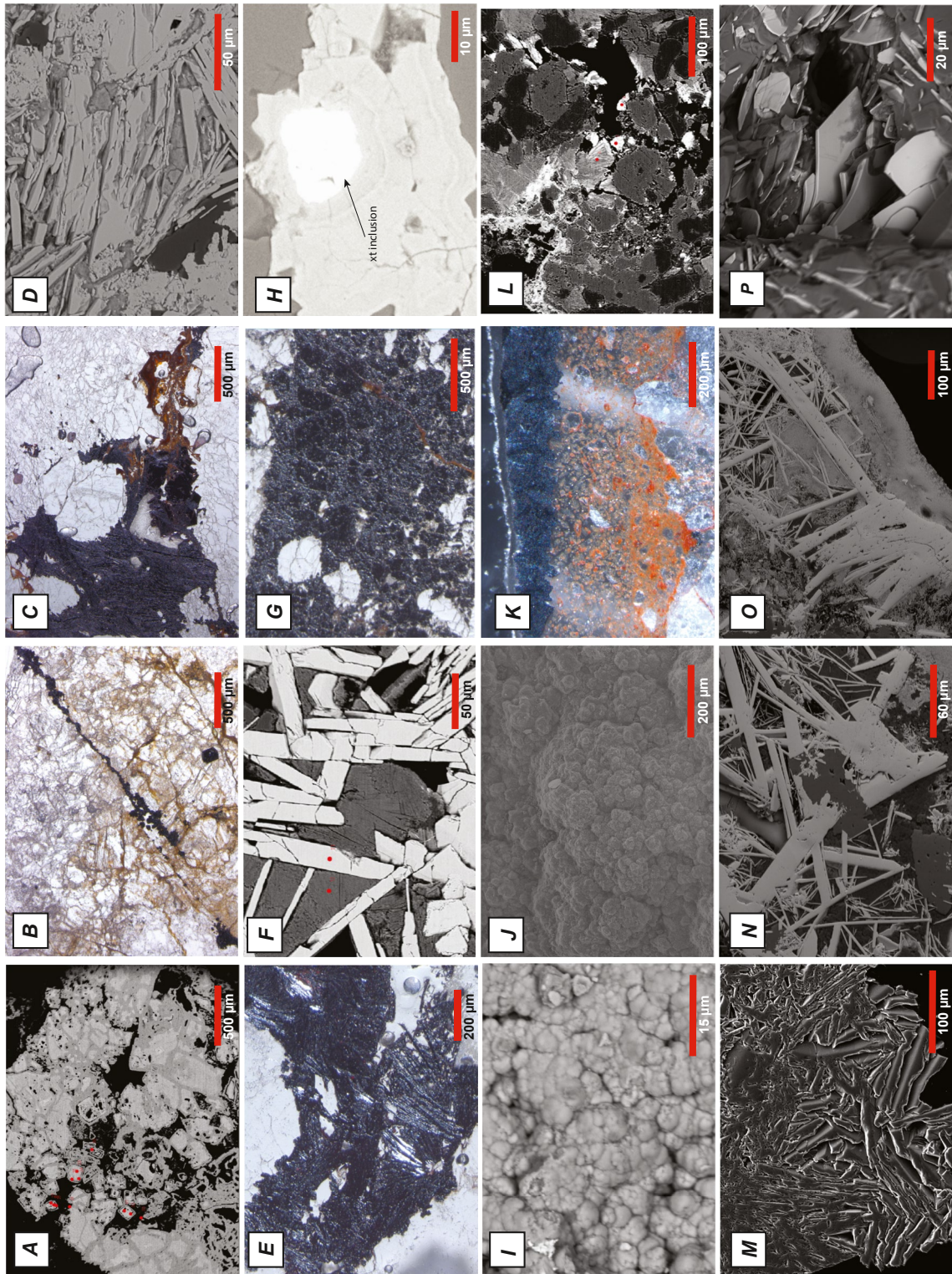


Figure 2.

### 3.1.2. Specular Hematite Blades

Sample GDTV-18 from the Catalina detachment fault zone comprises specular hematite blades up to 100  $\mu\text{m}$  long and 10  $\mu\text{m}$  wide in thick vein networks with microcrystalline Fe-Al hydroxides as impurities in hematite blades along with quartz and clay in grain matrices (Figure 2d). Sample LWTV-01 is from a quartz/hematite vein within fault breccia contains dispersed and undulating bands (possibly deformed) of specular hematite blades with dimensions ranging from 10 to 50  $\mu\text{m}$  in length and 5 to 10  $\mu\text{m}$  in width (Figure 2e). Sample LWTV-04 is a hematite coating on fracture/fault breccia with mylonitic clasts containing primary specularite with blade dimensions ranging from 10 to 50  $\mu\text{m}$  in width and 20 to 200  $\mu\text{m}$  in length (Figure 2f). Quartz fills voids in hematite blades which are accompanied by other Fe-oxide or hydroxide phases. Sample LWTV-09 is hematite from fault breccia with mylonitic clasts and has few specular blades approximately 10–50  $\mu\text{m}$  across but also exhibits regions of microcrystalline Fe-oxides filling voids between hematite blades (Figure 2g). Quartz and clay are also present between hematite crystals and few monazite grains approximately 20  $\mu\text{m}$  across are also present in this sample.

### 3.1.3. Botryoidal Oxides

Samples J107A and J107B were collected from the Catalina detachment fault zone on the north side of Tanque Verde Ridge and are siliceous fault rocks with sub-millimeter coatings or veins of hematite (Figure 2h and 2i). These samples comprise thin (<0.5 mm) coatings of dull, rusty hematite, though areas of metallic hematite are present in small quantities. Samples J107A and J107B have fine-grained lobes <1–15  $\mu\text{m}$  across and show evidence of compositional zonation in optical and BSE microscopy, largely controlled by Al and Fe content. Sample J107A contains an inclusion of xenotime approximately 25  $\mu\text{m}$  in width fully enclosed by hematite. Sample CH-3 is botryoidal hematite collected from fractures in sediments in the hanging wall of the Catalina detachment fault (Figure 2j). The Fe-oxide coating on sample CH-3 is < 2 mm thick and comprises relatively large and high purity lobes ranging 20–75  $\mu\text{m}$  across. Sample PRSB-01 is a Mn-oxide coating from a fracture in fault breccia with mylonitic clasts and comprises botryoidal lobes ranging 10–25  $\mu\text{m}$  across and regions of microcrystalline Mn-oxide with no discernable texture (Figure 2k). A small amount of Ba detected by EDS is evenly concentrated through the oxide layer.

### 3.1.4. Microcrystalline Mn-Oxides

Sample LWTV-02 is a Mn-oxide from a fracture surface with heterogeneous compositions throughout the sample including local enrichments of S and Cl (Figure 2l). Minor quartz and clay fill voids in the oxide layer. This sample appears to have crystals on a sub-micron scale, no individual crystals or textures are observable with optical or scanning electron microscopy.

## 3.2. Northern Galiuro Mountains

Fe- and Mn-oxides from Aravaipa Canyon in the Northern Galiuro Mountains were collected from fracture planes and quartz/hematite veins in Proterozoic rhyolite (Krieger, 1968, 1974). Sample NEAC1 is hematite

**Figure 2.** Backscatter (BSE), secondary electron (SE), and photomicrograph images of oxide samples. (a) Oxidized cubic morphologies in sample LWTV-03. (b) Oxide vein with cubic Fe-oxides in sample LWTV-06. (c) Metallic hematite increasingly oxidized to the edge of the vein in sample LWTV-08. (d) Specularite hematite blades in sample GDTV-18 from the Catalina detachment fault zone. (e) Specularite hematite blades in sample LWTV-01 from Tanque Verde Ridge. (f) Specularite hematite blades in sample LWTV-04 from Tanque Verde Ridge. (g) Specularite hematite blades and large metallic hematite grains in sample LWTV-09 from Tanque Verde Ridge. (h) Fine-grained botryoidal hematite and xenotime inclusion in sample J107A from the Catalina detachment fault zone. (i) Fine-grained botryoidal hematite in sample J107B from the Catalina detachment fault zone. (j) Coarse-grained botryoidal hematite in sample CH-3 from the hanging wall of the Catalina detachment fault. Coarse-grained botryoidal sample CH-3 yields older dates than finer-grained samples J107A and J107B. (k) Fine-grained botryoidal Mn-oxide in sample PRSB-01 from a fracture plane in the footwall of the Catalina detachment fault. (l) Microcrystalline Mn-oxide sample LWTV-02 from Tanque Verde Ridge. No crystal sizes or textures are evident from petrographic or spectroscopic analyses. (m) Specularite hematite blades in sample NEAC1 from a quartz/hematite vein in the Pinal Schist in the Galiuro Mountains. (n) Specularite hematite blades in sample NEAC3 from a fracture plane in the Pinal Schist in the Galiuro Mountains. (o) Fine-grained Mn-oxide in sample NEAC3T from a fracture plane in the Pinal Schist in the Galiuro Mountains. Sample NEAC3T shows the intergrowth of fine-grained Mn-oxide on top/toward the edge of the sample and coarse-grained hematite crystals (NEAC3) on the interior. (p) Specularite hematite blades in sample PH-1 from the footwall of the Pinalaño-Jackson Mountain metamorphic core complex.

collected from a quartz/hematite vein in 1.6 Ga rhyolite of the Pinal Schist and comprises specular hematite blades with dimensions of 10–50  $\mu\text{m}$  in width and 100–200  $\mu\text{m}$  in length within a quartz matrix (Figure 2m). Fe- and Mn-oxide samples NEAC3 and NEAC3T were collected from a fracture plane in the same rock type approximately two kilometers away. Sample NEAC3 comprises hematite blades with widths of <5–15  $\mu\text{m}$  and lengths ranging 10–150  $\mu\text{m}$  with interstitial quartz filling hematite voids (Figure 2n).

### 3.3. Pinaleño Mountains

Fe-oxides from Eagle Pass in the Pinaleño-Jackson Mountain core complex were collected adjacent to 26 Ma intrusive dikes and from fractures in the footwall near the Eagle Pass detachment fault (Nickerson, 2012). Sample PH-1 was collected from footwall fractures within the Eagle Pass detachment fault and comprises specular hematite blades with heterogeneous crystallite sizes with widths <5  $\mu\text{m}$  and lengths ranging from 5 to 50  $\mu\text{m}$  (Figure 2p). Additional phases from sample PH-1 include quartz and illite which fill voids in hematite blades. Samples EP027, EP034, EP069, and EP085 were collected from hematite veins and fracture planes close to 26 Ma dike intrusions, however, detailed spectroscopic and petrographic analyses beyond photomicrographs of analyzed aliquots for (U-Th)/He (Figures S2a–Sd in Supporting Information S1) are not available from these samples (Nickerson, 2012).

## 4. Methods

### 4.1. Petrography and Spectroscopy

We characterized crystallite size, morphology, and textural and compositional features of each sample with polished thin and/or thick sections at the University of Arizona with a Hitachi 3400N scanning electron microscope equipped with an Oxford EDS detector and a Leica MZ16 optical microscope. Chemical composition analyses and phase characterizations were completed with EDS whereas precise spot analyses and element maps were produced with a CAMECA SX100 electron probe microanalyzer to better quantify phase chemistry and improve textural analysis. Additional images of each sample, EDS spectra, and microprobe data are provided in Figures S1, S3 and S4 in Supporting Information S1.

### 4.2. (U-Th)/He Thermochronology

We measured U, Th, and He contents of all samples following procedures outlined by Evenson et al. (2014) and Garcia et al. (2018) at the University of Arizona. Aliquots for (U-Th)/He analysis were all interior fragments of larger polycrystalline aggregates ranging from 300 to 700  $\mu\text{m}$  in length and 100 to 400  $\mu\text{m}$  in length and width (see Supplementary Data File 1, Figure S2a–S2d in Supporting Information S1) for representative images of aliquots) with masses <0.5 mg. Aliquots were separated with a miniature drill, steel rod, or tweezers to remove fragments of oxide crystals from the parent rock. Aliquots were washed in pure water and then ethanol to remove detritus or contaminants. Cleaned aliquots were then dried and packed into 1-mm Nb tubes and placed into a copper planchet. Aliquots were degassed by diode or CO<sub>2</sub> lasers in a high vacuum extraction line at temperatures ranging from approximately 1000–1200 °C for 12–18 min, and then re-extracted for an equally long or longer duration at a higher laser power and temperature. Re-extractions of helium yielded fractions less than 2%–3% of initial release in all cases. <sup>4</sup>He abundance of aliquots was measured relative to a <sup>3</sup>He spike by quadrupole mass spectrometry following Reiners (2005). Degassed aliquots were then dissolved and analyzed for U and Th isotope concentrations by isotope dilution after the addition of a <sup>233</sup>U–<sup>229</sup>Th spike on a Thermo Fisher E2 ICP-MS.

Hofmann et al. (2020) showed that laser heating of some types of He-retentive hematite and goethite can result in U volatilization, resulting in (U-Th)/He dates of single-aliquot measurements with artificially low (U-Th)/He ratios and old dates. Our analyses were not performed with the high-*p*O<sub>2</sub> atmosphere method described by Hofmann et al. (2020) so the possibility exists that some samples may have experienced U volatilization, contributing to the dispersion of older (U-Th)/He dates in these samples. However, analytical procedures used here were similar to those used in our other studies in which we monitored changes in sample and elemental masses of volatile elements including Cu and Pb to avoid conditions leading to significant U-loss (Evenson et al., 2014; Garcia et al., 2018; Reiners et al., 2014). Although we cannot entirely rule out U-loss for some

samples, the fact that the dates of the most retentive hematite samples with (U-Th)/He dates of ca. 1.7–1.4 Ga and 1.1 Ga broadly overlap with crystallization ages of host rocks or nearby intrusions, is consistent with lack of significant U-loss.

### 4.3. $^4\text{He}/^3\text{He}$ Step Heating Experiments

In order to interpret He retention properties and the significance of (U-Th)/He ages, we performed  $^4\text{He}/^3\text{He}$  step-heating diffusion experiments on four aliquots from three samples from the Northern Galiuro Mountains. These included specular hematite from a quartz/hematite vein in 1.7–1.6 Ga rhyolite of the Pinal “Schist” (sample NEAC1C), two aliquots of specular hematite from a fracture in the same rhyolite (NEAC3B, NEAC3C), and one aliquot of the relatively fine-grained Mn-oxide (NEAC3T), found coating the previously mentioned sample (NEAC3C; Figure 2). Our  $^4\text{He}/^3\text{He}$  procedures followed methods described in Shuster et al. (2004; 2005), Evenson et al. (2014), and Garcia et al. (2018). Samples were irradiated with beam of  $\sim 200$  MeV protons for 5 hr and a total fluence of  $\sim 1 \times 10^{16}/\text{cm}^2$  at the Francis H. Burr Proton Therapy Center in Boston at the Massachusetts General Hospital. After irradiation,  $\sim 0.15$  mg of polycrystalline aliquots were placed in direct contact with a K-type thermocouple in vacuum and step-heated using a feedback-controlled laser diode; the  $^4\text{He}/^3\text{He}$  ratio and molar abundance of  $^3\text{He}$  in the evolved gas at each step was measured using an MAP-215 sector field mass spectrometer at the Berkeley Geochronology Center. Full analytical procedures for gas processing and mass spectrometry can be found in Tremblay et al. (2014).

### 4.4. Xenotime U-Pb Geochronology

A 25- $\mu\text{m}$  xenotime inclusion from hematite sample J107A was analyzed for U-Th-Pb content via LA-MC-ICP-MS at the Arizona Laserchron Center using a Teledyne Photon Machines G2<sup>TM</sup> solid state 193 nm NeF excimer laser paired with a Nu Instruments multicollector mass spectrometer. Data reduction follows the procedures outlined by Gehrels et al. (2008), Cecil et al. (2011), and Gehrels and Pecha (2014) using AGEcalc.

## 5. Results

(U-Th)/He dates of samples are reported as weighted averages with uncertainty reported at  $2\sigma$ , calculated by squaring the standard deviation of the (U-Th)/He aliquot dates and average analytical uncertainty of the (U-Th)/He aliquot dates, and taking the square root of the sum of the terms. (U-Th)/He data are summarized in Table 2. Figure 3 shows probability density plots of (U-Th)/He aliquots that highlight the distribution of sample and aliquot dates for geographic regions along the sampling transect. Figure 4 shows Arrhenius trends for step-heating results from samples NEAC1, NEAC3, and NEAC3T. Figure 5 displays step-age spectra results from these samples, and Figure 6 shows the modeled diffusion-domain sizes from step heating experiments from samples NEAC1, NEAC3, and NEAC3T. Table 3 shows the model parameters and bulk closure temperatures from the step-heating results. Figure 7 displays oxide (U-Th)/He aliquot and weighted mean dates plotted against distance along the regional transect. Hematite samples LWTV-01, LWTV-09, and GDTV-18 display slight negative date-eU correlations, however, other samples do not define a date-eU trend (Table S1 in Supporting Information S3).

### 5.1. Regional (U-Th)/He Date Trends

We observe the oldest (U-Th)/He dates from Proterozoic volcanic rocks in the Galiuro Mountains with hematite date distributions ca. 1.8–1.4 Ga and ca. 1.3–1.0 Ga. We observe Oligocene–Miocene (U-Th)/He dates from the footwall and hanging wall blocks of the Catalina-Rincon and Pinaleno-Jackson Mountain metamorphic core complexes with three prominent aliquot date clusters at ca. 24, 15, and 9 Ma (Figures 3b–3d). The youngest dates in this study (<5 Ma) are seen in the samples from brittle fractures in the footwall and the detachment fault zone of the Catalina-Rincon metamorphic core complex (Figure 3e).

**Table 2**  
*(U-Th)/He Data*

Sample/Aliquot	fmol He $\pm 2\sigma$	ng U $\pm 2\sigma$	ng Th $\pm 2\sigma$	Th/U	date (Ma)	$2\sigma \pm$ date (Ma)	$2\sigma \pm$ date %	Weighted mean date $\pm 2\sigma$ (Ma)	2 S.E. (Ma)
<b>Santa Catalina and Rincon Mountains</b>									
PRSB_01_1	32.18 $\pm$ 1.01	0.7426 $\pm$ 0.0215	0.0043 $\pm$ 0.0002	0.006	8.03	0.34	4.19	8.3 $\pm$ 0.4	0.3
PRSB_01_2	92.11 $\pm$ 2.63	2.0733 $\pm$ 0.0603	0.0227 $\pm$ 0.0009	0.011	8.22	0.33	4.00		
PRSB_01_3	43.79 $\pm$ 1.31	0.9438 $\pm$ 0.0273	0.0099 $\pm$ 0.0005	0.010	8.59	0.35	4.09		
J107A_1	0.68 $\pm$ 0.09	1.0274 $\pm$ 0.0294	0.4433 $\pm$ 0.0127	0.443	0.11	0.01	13.37	0.1 $\pm$ 0.02	0.01
J107A_2	0.58 $\pm$ 0.08	1.0066 $\pm$ 0.0289	0.5757 $\pm$ 0.0166	0.587	0.09	0.01	13.71		
J107A_3	0.90 $\pm$ 0.08	1.4385 $\pm$ 0.0413	0.4511 $\pm$ 0.0132	0.322	0.11	0.01	9.06		
J107A_4	0.58 $\pm$ 0.07	1.0686 $\pm$ 0.0306	0.6487 $\pm$ 0.0186	0.623	0.09	0.01	12.56		
J107A_5	0.50 $\pm$ 0.07	0.8623 $\pm$ 0.0247	0.2626 $\pm$ 0.0076	0.312	0.10	0.01	14.69		
J107B_1	2.17 $\pm$ 0.05	2.5722 $\pm$ 0.0741	0.6376 $\pm$ 0.0184	0.254	0.15	0.01	3.39	0.1 $\pm$ 0.3	0.3
J107B_2	0.82 $\pm$ 0.04	1.2723 $\pm$ 0.0366	0.6068 $\pm$ 0.0174	0.489	0.11	0.01	5.20		
J107B_3	0.96 $\pm$ 0.07	1.5226 $\pm$ 0.0435	0.6724 $\pm$ 0.0194	0.453	0.11	0.01	7.82		
J107B_4	0.83 $\pm$ 0.05	0.5717 $\pm$ 0.0163	0.2203 $\pm$ 0.0064	0.395	0.25	0.02	6.13		
J107B_5	6.93 $\pm$ 0.11	1.3274 $\pm$ 0.0379	0.4692 $\pm$ 0.0134	0.363	0.89	0.03	3.03		
GDTV_18_1	94.88 $\pm$ 0.65	1.3185 $\pm$ 0.0381	0.2803 $\pm$ 0.0080	0.218	12.71	0.35	2.74	13.5 $\pm$ 1.2	0.9
GDTV_18_2	82.17 $\pm$ 0.35	1.0167 $\pm$ 0.0293	0.3111 $\pm$ 0.0090	0.314	13.97	0.37	2.63		
GDTV_18_3	81.56 $\pm$ 0.36	0.9042 $\pm$ 0.0263	0.5584 $\pm$ 0.0159	0.633	14.59	0.37	2.51		
GDTV_18_4	75.45 $\pm$ 0.42	0.8247 $\pm$ 0.0239	0.4942 $\pm$ 0.0141	0.615	14.86	0.38	2.53		
GDTV_18_5	82.44 $\pm$ 0.42	1.0131 $\pm$ 0.0293	0.3483 $\pm$ 0.0099	0.353	13.95	0.37	2.63		
GDTV_18_6	75.95 $\pm$ 0.41	1.0784 $\pm$ 0.0310	0.4389 $\pm$ 0.0127	0.418	11.91	0.31	2.60		
CH_3_1	205.02 $\pm$ 9.01	1.4167 $\pm$ 0.0414	0.4550 $\pm$ 0.0130	0.329	24.92	1.28	5.13	24.2 $\pm$ 4.2	3.6
CH_3_2	237.53 $\pm$ 10.46	1.4377 $\pm$ 0.0410	0.2742 $\pm$ 0.0079	0.196	29.28	1.51	5.14		
CH_3_3	187.59 $\pm$ 8.26	1.2172 $\pm$ 0.0347	0.1486 $\pm$ 0.0044	0.125	27.74	1.43	5.16		
CH_3_4	226.32 $\pm$ 9.98	1.5206 $\pm$ 0.0441	0.2675 $\pm$ 0.0076	0.180	26.47	1.37	5.17		
CH_3_5	117.37 $\pm$ 5.22	1.0874 $\pm$ 0.0310	0.2777 $\pm$ 0.0079	0.262	18.87	0.97	5.15		
LWTV_01_1	18.35 $\pm$ 0.33	0.2058 $\pm$ 0.0059	0.0053 $\pm$ 0.0003	0.027	16.43	0.54	3.29	12.8 $\pm$ 4.4	3.1
LWTV_01_2	57.76 $\pm$ 0.95	0.6479 $\pm$ 0.0186	0.0084 $\pm$ 0.0004	0.013	16.48	0.53	3.21		
LWTV_01_4	85.66 $\pm$ 2.32	1.2605 $\pm$ 0.0589	0.0070 $\pm$ 0.0006	0.006	12.59	0.66	5.25		
LWTV_01_5	253.58 $\pm$ 6.86	2.0333 $\pm$ 0.0834	0.0067 $\pm$ 0.0006	0.003	23.09	1.11	4.79		
LWTV_01_6	87.05 $\pm$ 2.39	0.9742 $\pm$ 0.0388	0.0038 $\pm$ 0.0003	0.004	16.56	0.78	4.72		
LWTV_01_7	79.39 $\pm$ 0.78	1.5806 $\pm$ 0.0548	0.0113 $\pm$ 0.0094	0.007	9.30	0.32	3.47		
LWTV_01_8	105.55 $\pm$ 1.00	1.8042 $\pm$ 0.0556	0.0059 $\pm$ 0.0003	0.003	10.85	0.34	3.11		
LWTV_01_9	12.24 $\pm$ 0.25	0.1267 $\pm$ 0.0044	0.0022 $\pm$ 0.0006	0.018	17.84	0.70	3.91		
LWTV_02_1	0.81 $\pm$ 0.03	0.1557 $\pm$ 0.0045	0.1980 $\pm$ 0.0060	1.305	0.75	0.03	4.41	0.5 $\pm$ 0.3	0.3
LWTV_02_2	0.15 $\pm$ 0.02	0.0719 $\pm$ 0.0021	0.2140 $\pm$ 0.0063	3.051	0.22	0.03	14.46		
LWTV_02_3	0.22 $\pm$ 0.01	0.0517 $\pm$ 0.0015	0.1822 $\pm$ 0.0053	3.615	0.43	0.03	6.82		
LWTV_03_1	24.78 $\pm$ 0.34	1.7199 $\pm$ 0.0504	0.0390 $\pm$ 0.0013	0.023	2.66	0.08	3.12	3.0 $\pm$ 0.9	0.7
LWTV_03_2	34.60 $\pm$ 0.47	2.0342 $\pm$ 0.0586	0.0332 $\pm$ 0.0010	0.017	3.15	0.10	3.08		
LWTV_03_3	15.37 $\pm$ 0.22	1.0550 $\pm$ 0.0303	0.0262 $\pm$ 0.0008	0.025	2.69	0.08	3.11		
LWTV_03_4	65.94 $\pm$ 1.12	4.2116 $\pm$ 0.1258	0.0514 $\pm$ 0.0019	0.013	2.90	0.10	3.33		
LWTV_03_5	34.79 $\pm$ 0.69	1.6741 $\pm$ 0.0510	0.0100 $\pm$ 0.0006	0.006	3.85	0.14	3.54		
LWTV_03_6	76.06 $\pm$ 1.49	2.8977 $\pm$ 0.0891	0.0219 $\pm$ 0.0013	0.008	4.86	0.17	3.54		

**Table 2**  
*Continued*

Sample/Aliquot	fmol He $\pm 2\sigma$	ng U $\pm 2\sigma$	ng Th $\pm 2\sigma$	Th/U	date (Ma)	$2\sigma \pm$ date (Ma)	$2\sigma \pm$ date %	Weighted mean date $\pm 2\sigma$ (Ma)	2 S.E. (Ma)
LWTV_04_1	106.63 $\pm$ 0.86	0.8719 $\pm$ 0.0251	0.4564 $\pm$ 0.0130	0.537	20.17	0.53	2.62	14.9 $\pm$ 3.4	2.2
LWTV_04_2	218.62 $\pm$ 1.71	1.6620 $\pm$ 0.0486	1.6399 $\pm$ 0.0465	1.012	19.76	0.49	2.47		
LWTV_04_3	12.55 $\pm$ 0.16	0.1731 $\pm$ 0.0050	0.0352 $\pm$ 0.0011	0.208	12.84	0.38	2.96		
LWTV_04_7	75.34 $\pm$ 2.07	1.1230 $\pm$ 0.0470	0.1161 $\pm$ 0.0041	0.106	12.15	0.58	4.80		
LWTV_04_8	39.03 $\pm$ 1.08	0.4486 $\pm$ 0.0176	0.0466 $\pm$ 0.0020	0.107	15.75	0.73	4.62		
LWTV_04_9	57.78 $\pm$ 1.58	0.6997 $\pm$ 0.0292	0.0717 $\pm$ 0.0030	0.105	14.95	0.71	4.78		
LWTV_04_10	39.78 $\pm$ 0.79	0.4538 $\pm$ 0.0146	0.1121 $\pm$ 0.0038	0.253	15.36	0.54	3.54		
LWTV_04_11	20.77 $\pm$ 0.45	0.1925 $\pm$ 0.0089	0.0461 $\pm$ 0.0016	0.246	18.92	0.90	4.74		
LWTV_04_12	48.64 $\pm$ 1.05	0.7534 $\pm$ 0.0230	0.2191 $\pm$ 0.0079	0.298	11.20	0.39	3.51		
LWTV_06_1	0.15 $\pm$ 0.01	2.5786 $\pm$ 0.0740	0.0067 $\pm$ 0.0003	0.003	0.01	0.00	9.96	0.006 $\pm$ 0.003	0.01
LWTV_06_2	0.29 $\pm$ 0.02	10.3840 $\pm$ 0.2971	0.0114 $\pm$ 0.0004	0.001	0.01	0.00	7.57		
LWTV_06_3	0.06 $\pm$ 0.01	1.6979 $\pm$ 0.0488	0.0131 $\pm$ 0.0004	0.008	0.01	0.00	21.83		
LWTV_08_1	1.40 $\pm$ 0.04	0.5538 $\pm$ 0.0162	0.0228 $\pm$ 0.0008	0.042	0.46	0.02	3.79	0.1 $\pm$ 0.2	0.2
LWTV_08_2	0.34 $\pm$ 0.02	0.7445 $\pm$ 0.0213	0.0293 $\pm$ 0.0009	0.040	0.08	0.01	6.35		
LWTV_08_3	0.35 $\pm$ 0.02	0.4109 $\pm$ 0.0118	0.0051 $\pm$ 0.0002	0.013	0.16	0.01	5.74		
LWTV_09_1	20.08 $\pm$ 0.41	0.2641 $\pm$ 0.0076	0.3545 $\pm$ 0.0102	1.377	10.70	0.32	3.00	9.5 $\pm$ 1.0	0.8
LWTV_09_2	32.18 $\pm$ 0.61	0.4137 $\pm$ 0.0119	1.0286 $\pm$ 0.0293	2.550	9.08	0.25	2.79		
LWTV_09_3	46.00 $\pm$ 0.24	0.5636 $\pm$ 0.0162	0.9811 $\pm$ 0.0278	1.786	10.71	0.23	2.19		
LWTV_09_4	37.37 $\pm$ 0.80	0.5338 $\pm$ 0.0171	0.8875 $\pm$ 0.0302	1.706	9.31	0.30	3.23		
LWTV_09_5	56.54 $\pm$ 1.23	0.7216 $\pm$ 0.0223	2.3744 $\pm$ 0.0812	3.375	8.16	0.26	3.13		
LWTV_09_6	65.58 $\pm$ 1.05	0.8835 $\pm$ 0.0271	1.9298 $\pm$ 0.0621	2.241	9.07	0.25	2.75		
<b>Eagle Pass – Pinaleno Mountains</b>									
PH_1_1	59.23 $\pm$ 2.62	0.3654 $\pm$ 0.0104	1.7931 $\pm$ 0.0512	5.034	13.89	0.68	4.86	16.5 $\pm$ 6.0	6.0
PH_1_2	6.15 $\pm$ 0.06	0.0612 $\pm$ 0.0019	0.1237 $\pm$ 0.0035	2.075	12.61	0.31	2.46		
PH_1_3	55.24 $\pm$ 0.27	0.3331 $\pm$ 0.0095	0.3972 $\pm$ 0.0115	1.223	23.96	0.55	2.29		
PH_1_4	29.53 $\pm$ 0.21	0.1947 $\pm$ 0.0055	0.1737 $\pm$ 0.0050	0.915	23.19	0.56	2.43		
PH_1_5	5.96 $\pm$ 0.06	0.0996 $\pm$ 0.0029	0.4353 $\pm$ 0.0125	4.483	5.45	0.12	2.26		
EP027_1	12.87 $\pm$ 0.29	0.1500 $\pm$ 0.0044	0.1400 $\pm$ 0.0043	0.969	13.05	0.44	3.37	13.4 $\pm$ 1.3	1.1
EP027_2	8.29 $\pm$ 0.14	0.0800 $\pm$ 0.0025	0.0900 $\pm$ 0.0027	1.053	14.64	0.42	2.87		
EP027_3	36.67 $\pm$ 0.33	0.4000 $\pm$ 0.0132	0.3700 $\pm$ 0.0129	0.925	14.12	0.40	2.83		
EP027_4	14.81 $\pm$ 0.32	0.1700 $\pm$ 0.0052	0.1700 $\pm$ 0.0053	1.002	12.74	0.40	3.14		
EP027_6	7.20 $\pm$ 0.12	0.0900 $\pm$ 0.0057	0.1000 $\pm$ 0.0052	1.122	11.47	0.58	5.06		
EP034_1	77.21 $\pm$ 0.58	0.5700 $\pm$ 0.0191	0.5800 $\pm$ 0.0240	0.523	20.08	0.56	2.79	19.0 $\pm$ 4.0	1.5
EP034_2	92.11 $\pm$ 0.64	0.6400 $\pm$ 0.0231	0.5900 $\pm$ 0.0196	1.011	21.87	0.66	3.02		
EP034_3	151.93 $\pm$ 1.15	1.4200 $\pm$ 0.0708	0.4000 $\pm$ 0.0140	0.910	18.69	0.86	4.60		
EP034_4	52.47 $\pm$ 0.47	0.4300 $\pm$ 0.0132	0.3600 $\pm$ 0.0122	0.282	18.89	0.50	2.65		
EP034_5	64.84 $\pm$ 0.55	0.6700 $\pm$ 0.0300	0.2400 $\pm$ 0.0072	0.844	16.59	0.68	4.10		
EP034_6	62.03 $\pm$ 0.55	0.5800 $\pm$ 0.0207	0.3400 $\pm$ 0.0108	0.353	17.51	0.56	3.20		
EP069_1	8.38 $\pm$ 0.15	0.0700 $\pm$ 0.0019	0.3500 $\pm$ 0.0110	0.677	10.40	0.28	2.69	10.1 $\pm$ 0.9	0.7
EP069_2	3.60 $\pm$ 0.08	0.0300 $\pm$ 0.0010	0.1200 $\pm$ 0.0037	5.305	10.57	0.32	3.03		
EP069_3	4.54 $\pm$ 0.08	0.0300 $\pm$ 0.0008	0.2100 $\pm$ 0.0064	3.679	10.96	0.30	2.74		
EP069_5	2.46 $\pm$ 0.06	0.0243 $\pm$ 0.0007	0.1162 $\pm$ 0.0033	4.780	8.79	0.28	3.19		
EP069_6	4.87 $\pm$ 0.09	0.0385 $\pm$ 0.0011	0.2178 $\pm$ 0.0062	5.653	10.02	0.28	2.79		

**Table 2**  
*Continued*

Sample/Aliquot	fmol He $\pm 2\sigma$	ng U $\pm 2\sigma$	ng Th $\pm 2\sigma$	Th/U	date (Ma)	$2\sigma \pm$ date (Ma)	$2\sigma \pm$ date %	Weighted mean date $\pm 2\sigma$ (Ma)	2 S.E. (Ma)
EP085_1	9.52 $\pm$ 0.16	0.1400 $\pm$ 0.0040	0.2530 $\pm$ 0.0073	1.807	8.84	0.24	2.71	10.0 $\pm$ 2.4	1.9
EP085_2	71.10 $\pm$ 0.78	0.5561 $\pm$ 0.0199	1.3244 $\pm$ 0.0429	2.381	15.17	0.42	2.77		
EP085_3	5.80 $\pm$ 0.11	0.0684 $\pm$ 0.0020	0.1690 $\pm$ 0.0048	2.470	9.93	0.28	2.82		
EP085_4	6.26 $\pm$ 0.13	0.0746 $\pm$ 0.0021	0.1515 $\pm$ 0.0043	2.032	10.52	0.30	2.85		
EP085_5	8.91 $\pm$ 0.21	0.1154 $\pm$ 0.0033	0.2427 $\pm$ 0.0070	2.104	9.57	0.30	3.13		
EP085_6	4.78 $\pm$ 0.14	0.0662 $\pm$ 0.0019	0.1405 $\pm$ 0.0040	2.122	8.91	0.32	3.59		
<b>Aravaipa Canyon–Galiuro Mountains</b>									
NEAC1_1	3238.23 $\pm$ 95.22	0.2983 $\pm$ 0.0090	0.3602 $\pm$ 0.0113	1.239	1393.88	59.30	4.25	1534 $\pm$ 167	95
NEAC1_2	678.42 $\pm$ 15.46	0.0531 $\pm$ 0.0023	0.0673 $\pm$ 0.0027	1.300	1592.51	72.91	4.58		
NEAC1_3	2071.08 $\pm$ 54.51	0.1789 $\pm$ 0.0051	0.2207 $\pm$ 0.0069	1.266	1469.39	57.66	3.92		
NEAC1_5	2694.08 $\pm$ 76.18	0.2550 $\pm$ 0.0076	0.2302 $\pm$ 0.0073	0.926	1426.15	60.25	4.22		
NEAC1_6	3907.67 $\pm$ 45.96	0.3390 $\pm$ 0.0099	0.4108 $\pm$ 0.0125	1.243	1468.48	42.86	2.92		
NEAC1_7	4925.34 $\pm$ 82.32	0.3731 $\pm$ 0.0108	0.3377 $\pm$ 0.0097	0.928	1717.60	58.03	3.38		
NEAC1_8	1625.20 $\pm$ 27.64	0.1286 $\pm$ 0.0038	0.1061 $\pm$ 0.0031	0.846	1675.60	57.72	3.44		
NEAC1_9	2547.24 $\pm$ 36.69	0.1730 $\pm$ 0.0050	0.1779 $\pm$ 0.0051	1.055	1848.78	59.52	3.22		
NEAC1_10	3971.89 $\pm$ 31.81	0.2975 $\pm$ 0.0087	0.3094 $\pm$ 0.0089	1.067	1700.69	48.63	2.86		
NEAC1_11	1928.95 $\pm$ 14.63	0.1957 $\pm$ 0.0057	0.1428 $\pm$ 0.0044	0.749	1373.42	39.59	2.88		
NEAC1_12	3506.19 $\pm$ 50.97	0.3183 $\pm$ 0.0092	0.3094 $\pm$ 0.0089	0.997	1456.64	45.34	3.11		
NEAC3_2	4106.32 $\pm$ 17.39	0.6023 $\pm$ 2.9368	0.3668 $\pm$ 0.0111	0.625	1012.78	28.16	2.78	1138 $\pm$ 103	53
NEAC3_3	1761.33 $\pm$ 7.01	0.2578 $\pm$ 2.9907	0.1347 $\pm$ 0.0041	0.536	1030.64	29.65	2.88		
NEAC3_4	4954.80 $\pm$ 33.79	0.6274 $\pm$ 2.9095	0.4692 $\pm$ 0.0150	0.767	1129.55	31.52	2.79		
NEAC3_5	7370.68 $\pm$ 53.78	0.9855 $\pm$ 3.0511	0.7317 $\pm$ 0.0222	0.762	1076.33	31.30	2.91		
NEAC3_7	3342.82 $\pm$ 41.47	0.4059 $\pm$ 2.8744	0.3403 $\pm$ 0.0097	0.860	1150.59	33.92	2.95		
NEAC3_8	1391.34 $\pm$ 17.48	0.2068 $\pm$ 2.8723	0.0602 $\pm$ 0.0018	0.299	1055.78	33.66	3.19		
NEAC3_9	7463.47 $\pm$ 77.13	0.8850 $\pm$ 2.8728	0.4315 $\pm$ 0.0123	0.500	1246.88	37.89	3.04		
NEAC3_10	4849.74 $\pm$ 47.43	0.5953 $\pm$ 2.8946	0.3259 $\pm$ 0.0093	0.562	1196.82	35.75	2.99		
NEAC3_11	3224.15 $\pm$ 25.26	0.2724 $\pm$ 2.8710	0.1172 $\pm$ 0.0036	0.441	1684.96	52.65	3.12		
NEAC3_12	1487.47 $\pm$ 11.75	0.1657 $\pm$ 2.9077	0.0826 $\pm$ 0.0025	0.511	1314.76	39.38	3.00		
NEAC3_13	2760.93 $\pm$ 118.09	0.3271 $\pm$ 2.8657	0.1829 $\pm$ 0.0052	0.574	1232.48	68.24	5.54		
NEAC3B_14	1129.34 $\pm$ 7.58	0.1297 $\pm$ 0.1802	0.0901 $\pm$ 0.0027	0.712	1237.96	54.93	4.44		
NEAC3B_15	1468.51 $\pm$ 45.51	0.1040 $\pm$ 0.1662	0.0831 $\pm$ 0.0024	0.820	1844.73	86.14	4.67		
NEAC3B_16	1659.15 $\pm$ 11.33	0.1660 $\pm$ 0.4714	0.2357 $\pm$ 0.0068	1.456	1249.71	32.17	2.57		
NEAC3B_17	1132.34 $\pm$ 7.58	0.1331 $\pm$ 0.2649	0.1324 $\pm$ 0.0038	1.021	1154.96	31.12	2.69		
NEAC3T_1	68.69 $\pm$ 0.78	0.5811 $\pm$ 0.0167	0.0896 $\pm$ 0.0026	0.158	21.14	0.61	2.91	14.1 $\pm$ 12.7	9.0
NEAC3T_2	262.37 $\pm$ 2.99	2.2501 $\pm$ 0.0645	0.3084 $\pm$ 0.0088	0.141	20.93	0.61	2.91		
NEAC3T_3	200.86 $\pm$ 2.45	2.8865 $\pm$ 0.0823	0.1741 $\pm$ 0.0050	0.062	12.73	0.38	2.97		
NEAC3T_4	280.38 $\pm$ 3.22	1.4312 $\pm$ 0.0411	0.2151 $\pm$ 0.0062	0.154	35.02	1.02	2.92		
NEAC3T_5	7.90 $\pm$ 0.33	0.1376 $\pm$ 0.0040	0.0113 $\pm$ 0.0005	0.084	10.45	0.52	4.99		
NEAC3T_7	97.32 $\pm$ 3.06	0.9076 $\pm$ 0.0260	0.0613 $\pm$ 0.0018	0.069	19.57	0.81	4.17		
NEAC3T_8	14.24 $\pm$ 0.51	0.3370 $\pm$ 0.0097	0.0146 $\pm$ 0.0004	0.045	7.76	0.35	4.49		
NEAC3T_9	298.93 $\pm$ 9.51	1.2108 $\pm$ 0.0350	0.0832 $\pm$ 0.0024	0.070	44.93	1.89	4.22		

Note. (U-Th)/He data for individual aliquots. Strikethrough entries are outlier aliquots not included in the weighted mean calculation.

### 5.2. Northern Galiuro Mountains Samples

Hematite from the northern Galiuro Mountains display Proterozoic (U-Th)/He date populations and Mn-oxide aliquots from this region display a distribution of Eocene–Miocene dates. Hematite sample NEAC1 yields a range of aliquot dates of 1849–1373 Ma and a weighted mean date of  $1534 \pm 167$  Ma ( $n = 11$ ) with a bimodal aliquot date distribution with peaks at 1.68 Ga and 1.44 Ga. Hematite sample NEAC3 yields a range of aliquot dates of 1315–1013 Ma and a weighted mean date of  $1138 \pm 103$  Ma ( $n = 13$ ). Mn-oxide sample NEAC3T yields a range of aliquot dates of 45–8 Ma and a weighted mean date of  $14.1 \pm 12.7$  Ma ( $n = 8$ ; Figure 3a). Th/U values of hematite samples NEAC1 and NEAC3T range from 0.3 to 1.5 and Th/U values of Mn-oxide NEAC3T range from 0.04 to 0.16.

### 5.3. Santa Catalina-Rincon Metamorphic Core Complex Samples

Oxide samples from the Catalina and Rincon Mountains display two main date populations. The first subset yield Miocene with a few late-Oligocene aliquot dates. Fe-oxide samples LWTV-01, LWTV-04 and LWTV-09 from the footwall of the Catalina detachment fault yield a range of aliquot dates of 23–9 Ma and a weighted mean of  $12.8 \pm 4.4$  Ma ( $n = 8$ ), 20–11 Ma and  $14.9 \pm 3.4$  Ma ( $n = 9$ ), and 11–8 Ma and  $9.4 \pm 1.0$  Ma ( $n = 6$ ), respectively. Sample GDTV-18 from the Catalina detachment fault zone yields a range of aliquots dates of 15–12 Ma and a weighted mean date of  $13.5 \pm 1.2$  Ma ( $n = 6$ ). Mn-oxide sample PRSB-01 from the footwall of the Catalina detachment fault yields aliquot dates ca. 8 Ma, with aliquots within uncertainty of each other and a weighted mean date of  $8.3 \pm 0.4$  Ma ( $n = 3$ ). Sample CH-3 from the hanging wall of the Catalina detachment faults yields a range of aliquot dates of 29–19 Ma and a weighted mean date of  $24.2 \pm 4.2$  Ma ( $n = 5$ ; Figure 3c). A xenotime inclusion in hematite sample J107A yields a  $^{238}\text{U}$ – $^{206}\text{Pb}$  date of  $23.3 \pm 2.9$  Ma ( $n = 1$ ; Figure 2c, Table S4 in Supporting Information S3). The second subset of dates is much younger, comprising fine-grained botryoidal and recrystallized or pseudomorphically replaced oxides. Botryoidal hematites from samples J107A and J107B from the Catalina detachment fault zone yield a range of aliquot dates of 0.1–0.09 Ma and a weighted mean date of  $0.1 \pm 0.02$  Ma ( $n = 5$ ), and 0.9–0.1 Ma ( $n = 5$ ). Samples located within or close to pronounced SE–NW fractures on Tanque Verde Ridge in the Rincon Mountains include Mn-oxide sample LWTV-02, and oxidized/recrystallized Fe-oxide samples LWTV-03, LWTV-06, and LWTV-08. Sample LWTV-02 yields a range of aliquot dates of 0.8–0.2 Ma and a weighted mean of  $0.5 \pm 0.3$  Ma ( $n = 3$ ). Recrystallized Fe-oxide samples LWTV-03, LWTV-06, and LWTV-08 yield a range of aliquots dates of 5–3 Ma and a weighted mean date of  $3.0 \pm 0.9$  Ma ( $n = 6$ ), 0.01 Ma ( $n = 3$ ), and 0.5–0.1 Ma ( $n = 3$ ), respectively (Figure 3e). Recrystallized samples LWTV-03, LWTV-06, and LWTV-08 yield Th/U values  $< 0.04$ , while Mn-oxide samples PRSB-01 and LWTV-02 yield Th/U values of 0.006–3.6. Samples that comprise specular and botryoidal hematite from this region yield Th/U values of 0.003–3.4.

### 5.4. Pinaleño Mountains Samples

Fe-oxides from the footwall of the Eagle Pass and Pinaleño detachment faults have Oligocene–Miocene dates similar to those from the Catalina-Rincon core complex (Figure 3b). Sample PH-1 from cataclastic fault rocks yields a range of aliquot dates of 24–5 Ma and a weighted mean date of  $16.5 \pm 6.0$  Ma ( $n = 5$ ). Sample EP069 from a shear zone approximately 10 km north of the Eagle Pass detachment fault yields a range of aliquot dates of 11–9 Ma and a weighted mean date of  $10.1 \pm 0.9$  Ma ( $n = 5$ ). Samples EP027, EP034, and EP085 from within the Eagle Pass dike swarm yield a range of aliquot dates of 49–11 Ma and a weighted mean date of  $13.4 \pm 1.3$  Ma ( $n = 6$ ), 22–17 Ma and a weighted mean date of  $19.0 \pm 4.0$  Ma ( $n = 6$ ), and 15–9 Ma with a weighted mean date of  $10.0 \pm 2.4$  Ma ( $n = 6$ ), respectively (Figure 3d). Hematite samples from this region yield Th/U values of 0.3–7.0 with the younger samples (EP069 and EP085) tending to have higher Th/U compared to older samples (EP027, EP034, and PH-1).

### 5.5. $^4\text{He}/^3\text{He}$ Step-Heating Results

Fe-oxide samples NEAC1 and NEAC3 and Mn-oxide sample NEAC3T from the Galiuro Mountains were selected for  $^4\text{He}/^3\text{He}$  step heating experiments. Fe-oxide samples are coarse-grained and EPMA results suggest relatively homogeneous crystallites. Mn-oxide sample NEAC3T was selected for its relationship to NEAC3

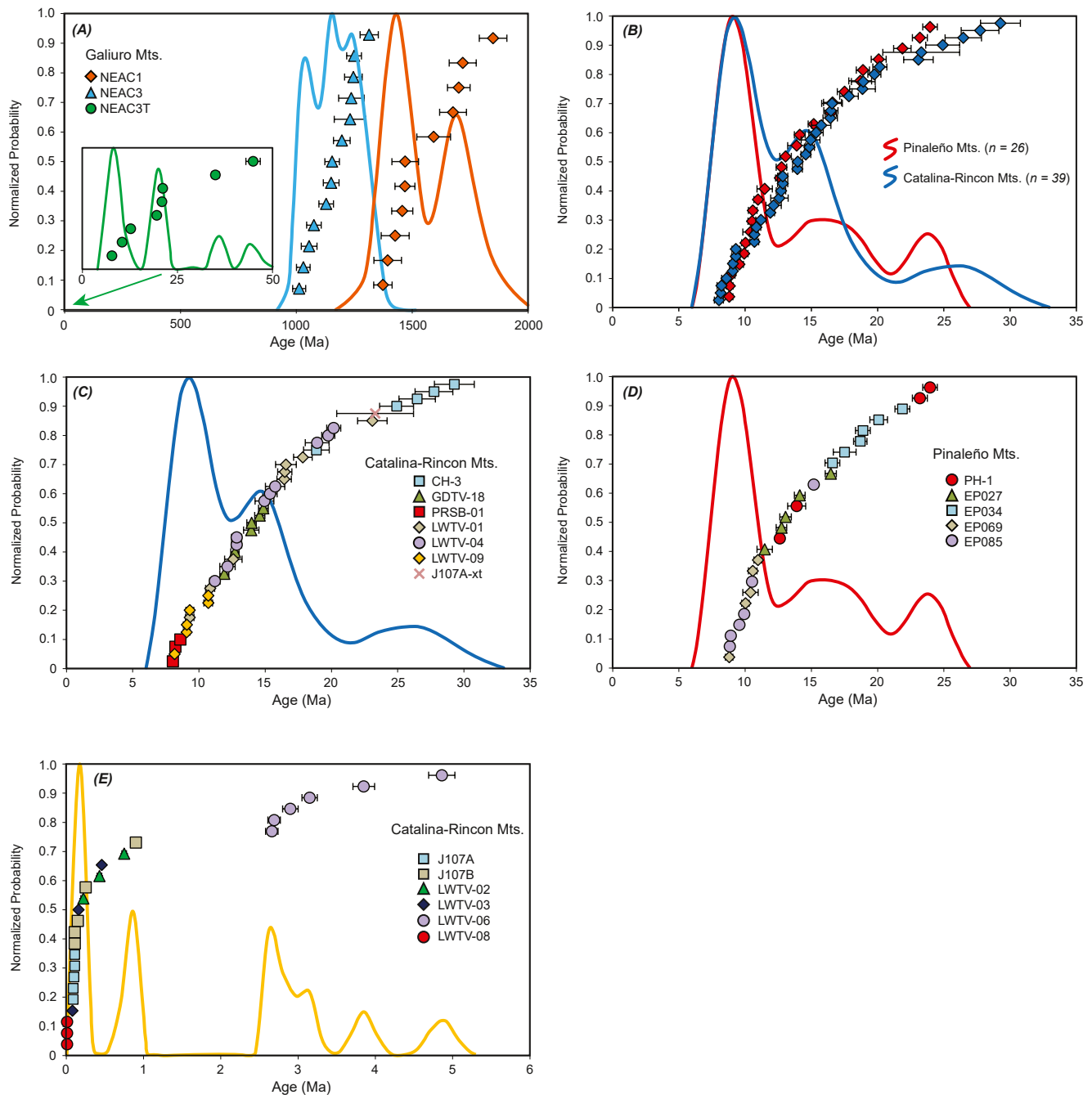


**Figure 3.** (a) Probability density plot (PDP) of Galiuro Mountains samples NEAC1 (orange line and diamonds), NEAC3 (blue line and triangles), and NEAC3T (green line and circles). Hematite sample NEAC1 shows bimodal date distributions at ca. 1.7 and 1.4 Ga. Hematite sample NEAC3 shows a continuum of dates from 1.3 to 1.0 Ga. Mn-oxide sample NEAC3T shows date populations of 45–8 Ma. (b) PDP of individual aliquot dates from the Catalina-Rincon (blue line and diamonds) and Pinalaño Mountains (red line and diamonds) plotted together. Individual aliquots from these ranges cluster into three prominent date distributions at ca. 25–24 Ma, 16–14 Ma, and 10–9 Ma. (c) PDP of Fe- and Mn-oxide aliquots from the Catalina and Rincon Mountains discriminated by sample. (d) PDP of Fe-oxide aliquots from the Pinalaño Mountains discriminated by sample. (e) PDP of microcrystalline and recrystallized Fe- and Mn-oxides from Tanque Verde Ridge. A majority of aliquots yield dates < 1 Ma, one sample (LWTV-03) yields dates < 5 Ma. All of these samples display evidence of recrystallization or pseudomorphic replacement and/or sub-micron crystallite sizes. Error bars on aliquot dates are  $2\sigma$ .

**Table 3**

Activation Energies, ( $E_a$ ),  $\ln(D_0/a^2)$ , and Diffusion Domain Size  $a$ , and Closure Temperatures ( $T_{c10}$  Assuming  $10^\circ\text{C}/\text{Ma}$  Cooling Rate) Implied by Assumed  $D_0$  for Inverse and Forward Models of  $^3\text{He}$  Step-Heating Release Experiments

Sample	Descrip.	Model type	Kinetics	$E_a$ [kJ/mol]	$D_0$ assumed for calculating $a$ [ $\text{cm}^2/\text{s}$ ]	$\ln(D_0/a^2)$ and corresponding fractions and implied $a$ for each domain				Bulk predicted $T_{c10}$ [ $^\circ\text{C}$ ]	cumulative residuals [ $\text{s}^{-1}$ ]
						$\ln(D_0/a^2)$ [ $\ln \text{s}^{-1}$ ]	fraction	implied $a$ [ $\mu\text{m}$ ]	$T_{c10}$ [ $^\circ\text{C}$ ]		
11NEAC1C	Qtz-vein hematite	Inverse, 4 domains	Farley (2018)	171	0.5168	$\ln(D_0/a^2)$ [ $\ln \text{s}^{-1}$ ]	fraction	implied $a$ [ $\mu\text{m}$ ]	$T_{c10}$ [ $^\circ\text{C}$ ]	234	0.546
						27.50	0.030	7.68e-3	59		
						14.75	0.035	4.506	141		
						9.500	0.095	62.21	188		
						4.000	0.840	973.1	249		
11NEAC1C	Qtz-vein hematite	Forward, 5 domains	Farley (2018)	171	0.5168	$\ln(D_0/a^2)$ [ $\ln \text{s}^{-1}$ ]	fraction	implied $a$ [ $\mu\text{m}$ ]	$T_{c10}$ [ $^\circ\text{C}$ ]	227	1.04
						36.18	0.010	0.0001	19		
						22.36	0.040	0.100	88		
						8.550	0.050	100	197		
						7.164	0.300	200	212		
						3.945	0.600	1000	250		
11NEAC1C	Qtz-vein hematite	Inverse, 4 domains	Evenson et al. (2014)	148.5	2.20e-4	$\ln(D_0/a^2)$ [ $\ln \text{s}^{-1}$ ]	fraction	implied $a$ [ $\mu\text{m}$ ]	$T_{c10}$ [ $^\circ\text{C}$ ]	199	0.382
						30.00	0.010	4.54e-5	3		
						18.00	0.025	0.01830	64		
						7.500	0.135	3.488	144		
						1.000	0.830	89.96	215		
11NEAC1C	Qtz-vein hematite	Forward, 5 domains	Evenson et al. (2014)	148.5	2.20e-4	$\ln(D_0/a^2)$ [ $\ln \text{s}^{-1}$ ]	fraction	implied $a$ [ $\mu\text{m}$ ]	$T_{c10}$ [ $^\circ\text{C}$ ]	196	0.804
						28.42	0.010	0.0001	10		
						14.60	0.040	0.100	86		
						5.394	0.050	10	164		
						4.007	0.300	20	179		
						0.7885	0.600	100	217		
11NEAC3B	Fracture-fill hematite	Inverse, 4 domains	Farley (2018)	171	0.5168	$\ln(D_0/a^2)$ [ $\ln \text{s}^{-1}$ ]	fraction	implied $a$ [ $\mu\text{m}$ ]	$T_{c10}$ [ $^\circ\text{C}$ ]	228	7.48
						37.00	0.010	6.64e-5	16		
						27.00	0.030	0.00986	61		
						12.00	0.215	17.83	16		
						3.500	0.745	1250	256		

**Table 3**

*Continued*

11NEAC3B	Fracture-fill hematite	Inverse, 4 domains	Evenson et al. (2014)	148.5	2.20e-4	$\ln(D_0/a^2)$ [ln s <sup>-1</sup> ]	fraction	implied $a$ [μm]	$T_{c10}$ [°C]	187	60.8
						32.00	0.010	1.67e-5	-5		
						22.00	0.030	0.00248	41		
						8.500	0.215	2.116	134		
						1.500	0.745	70.063	208		
11NEAC3B	Fracture-fill hematite	Forward, 5 domains	Evenson et al. (2014)	148.5	2.20e-4	$\ln(D_0/a^2)$ [ln s <sup>-1</sup> ]	fraction	implied $a$ [μm]	$T_{c10}$ [°C]	189	62.6
						28.42	0.020	0.0001	10		
						19.21	0.050	0.01	57		
						10.00	0.040	1	121		
						5.394	0.15	10	164		
						1.235	0.740	80	212		
11NEAC3C	Fracture-fill hematite	Forward, 5 domains	Evenson et al. (2014)	148.5	2.20e-4	$\ln(D_0/a^2)$ [ln s <sup>-1</sup> ]	fraction	implied $a$ [μm]	$T_{c10}$ [°C]	189	33.5
						28.42	0.020	0.0001	10		
						14.60	0.050	0.01	57		
						5.394	0.040	1	121		
						4.007	0.15	10	164		
						0.7885	0.740	80	212		
11NEAC3T	Fracture-fill Mn-oxide	Forward, 5 domains	Lippolt and Hautmann (1995) as cited in Evenson et al. (2014)	134	3.981e-3	$\ln(D_0/a^2)$ [ln s <sup>-1</sup> ]	fraction	implied $a$ [μm]	$T_{c10}$ [°C]	24	0.96
						26.71	0.35	0.001	-9		
						22.10	0.25	0.01	12		
						17.50	0.20	0.10	36		
						12.89	0.10	1.0	65		
						8.299	0.10	10	100		

and distinct chemical and morphological characteristics from NEAC1 and NEAC3. Results of <sup>4</sup>He/<sup>3</sup>He step heating experiments are summarized in Table 3 and Figure 4. All samples were subjected to between four and five pro- and retrograde cycles of heating between temperatures of 120 and 800 °C; several samples also included steps at 900–1150 °C. Final degassing, confirmed with zero re-extraction on subsequent steps, was achieved at 1150–1300 °C, with the exact temperature depending on the sample. Figure 4 shows Arrhenius trends for release of <sup>3</sup>He and <sup>4</sup>He, along with characteristics of multidomain models used for interpreting the He retention properties and (U-Th)/He ages in subsequent sections. All samples showed complex Arrhenius trends for the initially homogeneously distributed <sup>3</sup>He, similar to results from previous polycrystalline Fe- and Mn-oxide samples (Evenson et al., 2014; Farley & Flowers, 2012; Farley & McKeon, 2015; Garcia et al., 2018), with apparently decreasing diffusivity with progressive degassing. All samples also show apparently higher <sup>3</sup>He than <sup>4</sup>He diffusivities in the early stages of degassing, but converging apparent

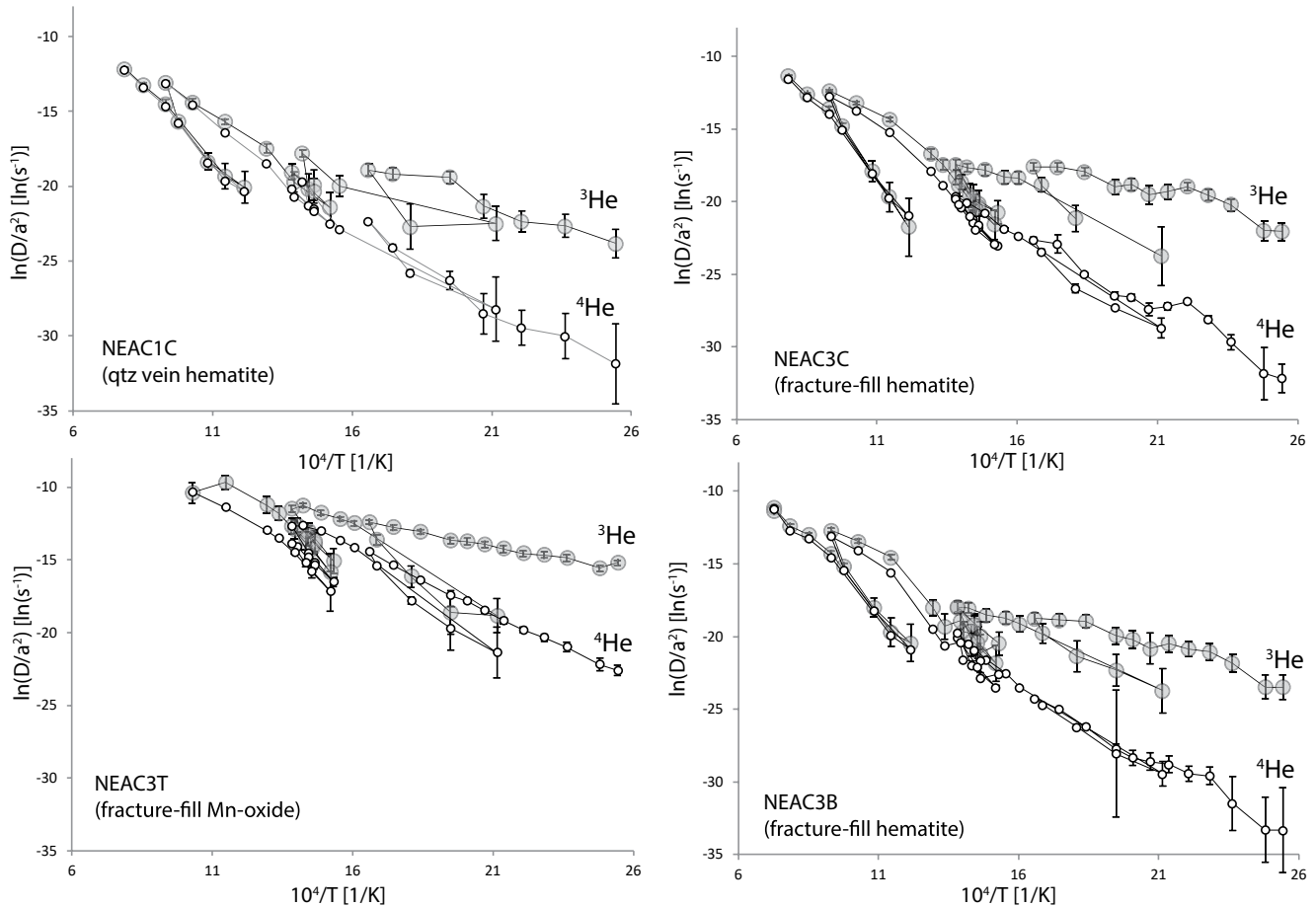


**Figure 4.** Arrhenius trends for step-heating results of  $^4\text{He}/^3\text{He}$  experiments on four samples from the Galiuro Mountains. Large gray symbols are  $^3\text{He}$  and small open symbols are  $^4\text{He}$ . Apparent diffusivity of  $^3\text{He}$  is higher than that of  $^4\text{He}$  in initial steps for all samples. Behavior of the two aliquots for the fracture-fill specularite NEAC3B and NEAC3C are similar. Both isotopes show apparently higher diffusivity in the NEAC3T Mn-oxide. Error bars on  $\ln(D/a^2)$  values are  $2\sigma$  and were calculated following the procedures outlined for error propagation during step-heating experiments for a spherical geometry in Ginster and Reiners (2018). Error bars may be smaller than the symbol for some steps. The uncertainty on  $\ln(D/a^2)$  values include the cumulative effects of converting the current step and each previous steps' fractional loss to diffusivity. Uncertainty on temperature values are approximately two large circle diameters at low-T steps, and smaller than the symbol for high-T steps.

diffusivities for the two isotopes in later stages of the experiments. The two aliquots of hematite from the same sample (NEAC3B and NEAC3C) showed very similar Arrhenius trends.

## 6. Discussion

### 6.1. Interpretations of $^4\text{He}/^3\text{He}$ Step-Heating Results

#### 6.1.1. Step-Age Spectra

Assuming a uniform distribution of parent nuclides (U, Th) in the aliquots used for step-heating experiments, variations in  $^4\text{He}$  content within each aliquot can be interpreted to represent varying amounts of diffusive loss from domains with varying He retentivity. Therefore, changes in  $^4\text{He}/^3\text{He}$  through a step-heating experiment can be used to create step-age evolution plots analogous to those of  $^{40}\text{Ar}/^{39}\text{Ar}$  step-heating experiments (e.g., Farley & Flowers, 2012; Farley & McKeon, 2015), by multiplying the bulk (U-Th)/He age of a sample (determined from the weighted mean age of multiple aliquots of that sample) by  $(^4\text{He}/^3\text{He})_{\text{step}} / (^4\text{He}/^3\text{He})_{\text{bulk}}$ , and plotting this as a function of cumulative  $^3\text{He}$  released (Figure 5). The contribution of low-retentivity domains to the bulk  $^4\text{He}$  content and therefore age is seen in the early, low cumulative  $^3\text{He}$  portions of the step-age spectra. Assuming negligible compositional/mineralogical heterogeneity from

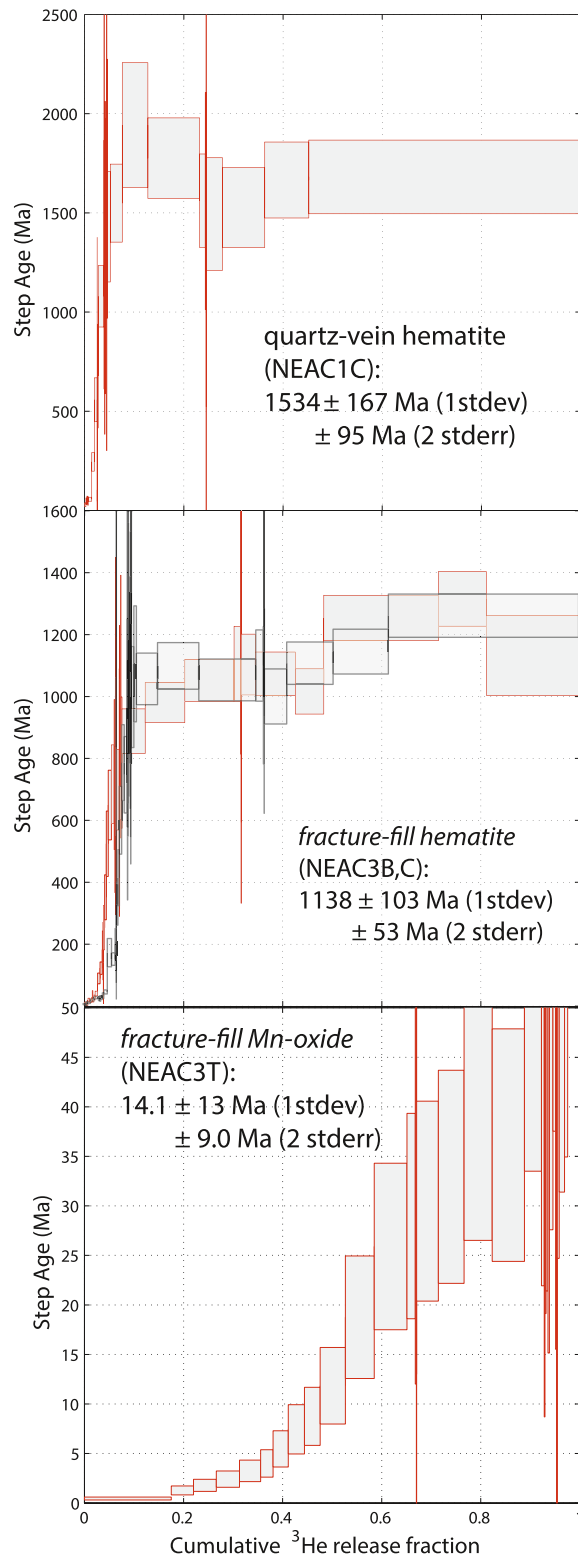


Figure 5.

these samples, a likely explanation for the low retentivity of these domains is that they are smaller (lower effective  $D/a^2$ ) than domains that contribute larger fractions of  $^4\text{He}$  in later steps. Similar step-ages across a large range of cumulative  $^3\text{He}$  may be interpreted as representing domains with relatively uniform concentrations of  $^4\text{He}$ , such as those that have lost little  $^4\text{He}$  since formation or an episode of cooling from high-temperature.

In this context, the step-age spectra of the Galiuro Mountains hematite samples are similar in showing relatively young ages, implying low retentivity, for the first 5%–10% of the spectrum, followed by a broad but imprecise plateau age of Proterozoic ages over about 85%–90% of the  $^3\text{He}$  release, likely representing  $^4\text{He}$  from domains that experienced relatively little  $^4\text{He}$  loss. For the quartz/hematite-vein hematite sample NEAC1, this plateau is roughly 1.8–1.5 Ga, similar to the age of widely-distributed and proximal rhyolitic volcanics in the region (and this sample's host rock) of  $\sim 1.65$  Ga (Bickford et al., 2019; Eisele & Isachsen, 2001; Meijer, 2014). For the fracture-fill hematite sample NEAC3, the plateaus of the two aliquots are similar at about 1.3–1.0 Ga, similar to the age of widespread diabase in southern and central Arizona that is likely the same as this sample's host rock (Bright et al., 2014). Taken together, these results are consistent with formation of these hematite samples at approximately the same time as formation of their host rocks, and loss of about 5%–10% of  $^4\text{He}$  from relatively unretentive domains (possibly small crystallites) since then. In contrast to the hematite samples, the Mn-oxide sample NEAC3T, overlying of fracture-filling hematite NEAC3 (on the interior side of the fracture), shows no plateau in the step-age spectrum. The consistent increase of apparent step-age with cumulative  $^3\text{He}$  for this sample suggests extensive  $^4\text{He}$  loss from domains with a spectrum of  $^4\text{He}$  retentivity, with no indication of a single plateau that would be used to constrain timing of formation or cooling from high temperatures beyond the maximum step-age observed.

### 6.1.2. Diffusion Domain Modeling

In order to understand the diffusion domain characteristics within the Galiuro hematite and Mn-oxide samples, we modeled the observed  $^3\text{He}$  release using both forward and inverse methods. Following similar multi- or “poly-”domain approaches for Ar and He (e.g., Farley & Flowers, 2012; Farley & McKeon, 2015; Lovera et al., 1991), for each model we assume a single activation energy but varying  $D_0/a^2$  among spherical domains containing varying proportions of  $^3\text{He}$ . Our forward models, in which we attempted to create  $^3\text{He}$  Arrhenius trends qualitatively similar to those observed by manually changing  $D_0/a^2$  and fractions of domains, used five domains, though overall fits and residuals (Figures S5–S8 in Supporting Information S2) were not substantially better than for models with four domains. Our inverse models used four domains, as this was found to provide significantly better fits to the observed trends than three, but nearly as good as five. For hematite we assumed two different activation energies,  $E_a$ . The first is 171 kJ/mol, from single-crystal  $^3\text{He}$  diffusion experiments of Farley (2018); the second is 148.5 kJ/mol, from  $^3\text{He}$  diffusion experiments on poly-domain hematite samples (Evenson et al., 2014). Each of these studies also proposed values for frequency factor,  $D_0$ , based on different approaches. Farley (2018) proposed  $0.5168 \text{ cm}^2/\text{s}$ , from experiments on varying size fragments of single crystals, whereas Evenson et al. (2014) proposed  $2.20 \times 10^{-4}$ , based on correlation between observed inverse square of estimated crystal size and apparent  $D_0/a^2$  among  $^4\text{He}$  and  $^3\text{He}$  in nine diffusion experiments from four studies (Bähr et al., 1994; Evenson et al., 2014; Farley & Flowers, 2012; Lippolt et al., 1993). For Mn-oxide we used He diffusion kinetics of Lippolt and Hautmann (1995), as cited in Evenson et al. (2014), with  $E_a$  of 134 kJ/mol, and  $D_0$  of  $3.981 \times 10^{-3} \text{ cm}^2/\text{s}$ .

Fractions and  $\ln(D_0/a^2)$  for all models are shown in Table 3. In all cases, inverse models yield lower residuals (better fit; see Figures S5–S8 in Supporting Information S2) than forward models, despite the fact that the forward models use five domains instead of the inverse models' four, however the difference for sample NEAC3B is insignificant. Both inverse and forward models were run using both Evenson and Farley kinetics

**Figure 5.** Step-age spectra based on  $^4\text{He}/^3\text{He}$  release experiments for samples from the Galiuro Mountains. The middle panel includes results from two different step-heating experiments on separate aliquots from the same sample. Other panels represent results from a single aliquot from each sample. Dates reported in each panel are weighted mean dates from multiple aliquots of each sample, with uncertainties, used as the normalizing age in the step-age plots. Relatively young dates at low  $^3\text{He}$  release fraction are interpreted as domains/crystallites that have lost  $^4\text{He}$  by diffusion since formation. The hematite samples show young dates for the first 5%–10% of  $^3\text{He}$  released, followed by steps between about 1.8 and 1.5 Ga (NEAC1C) or 1.3 and 1.0 Ga (NEAC3B, C). Note that y-axes have been trimmed to display the age plateaus, and uncertainties are not fully shown for samples that contain steps with large uncertainties. Uncertainty for step-age boxes were calculated by incorporating uncertainty of  $^3\text{He}$ ,  $^4\text{He}$ , and blank measurements, as well as the bulk sample age.

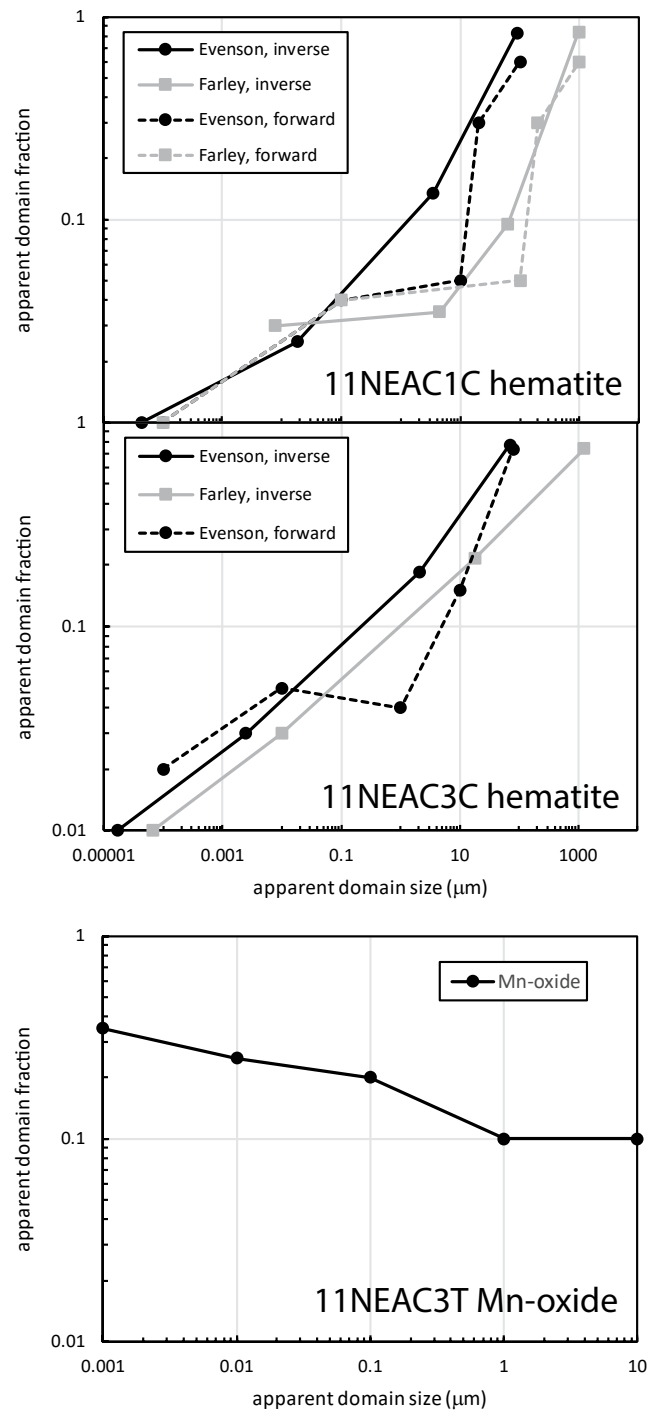


**Figure 6.** Relationships between model fractions and apparent length scales (size) of predicted diffusion domains in polydomain diffusion models based on  $^3\text{He}$  step-heating experiments, for NEAC1C (quartz/hematite vein in 1.65 Ga rhyolite) and NEAC3C (fracture fill hematite in 1.1 Ga diabase), and NEAC3T (Mn-oxide coating NEAC3C in fracture fill). Hematite models were run by inverse and forward methods using activation energies ( $E_a$ ) and frequency factors ( $D_0$ ) for He diffusion from either Farley (2018) or Evenson et al. (2014) (although a forward model for Farley kinetics was not run for sample NEAC3C). Mn-oxide model was run by forward methods only, using He diffusion kinetics of Lippolt and Hautmann (1995) as cited in Evenson et al. (2014). Hematite models all predict positive correlations between domain fraction and size, with 85%–90% of  $^3\text{He}$  residing in domains tens of microns in size (or hundreds of microns for the Farley kinetics). The Farley  $D_0$  leads to significantly larger predicted diffusion domain sizes than the Evenson  $D_0$ . The Mn-oxide model predicts an inverse correlation between domain fraction and size and much smaller differences in domain fractions.

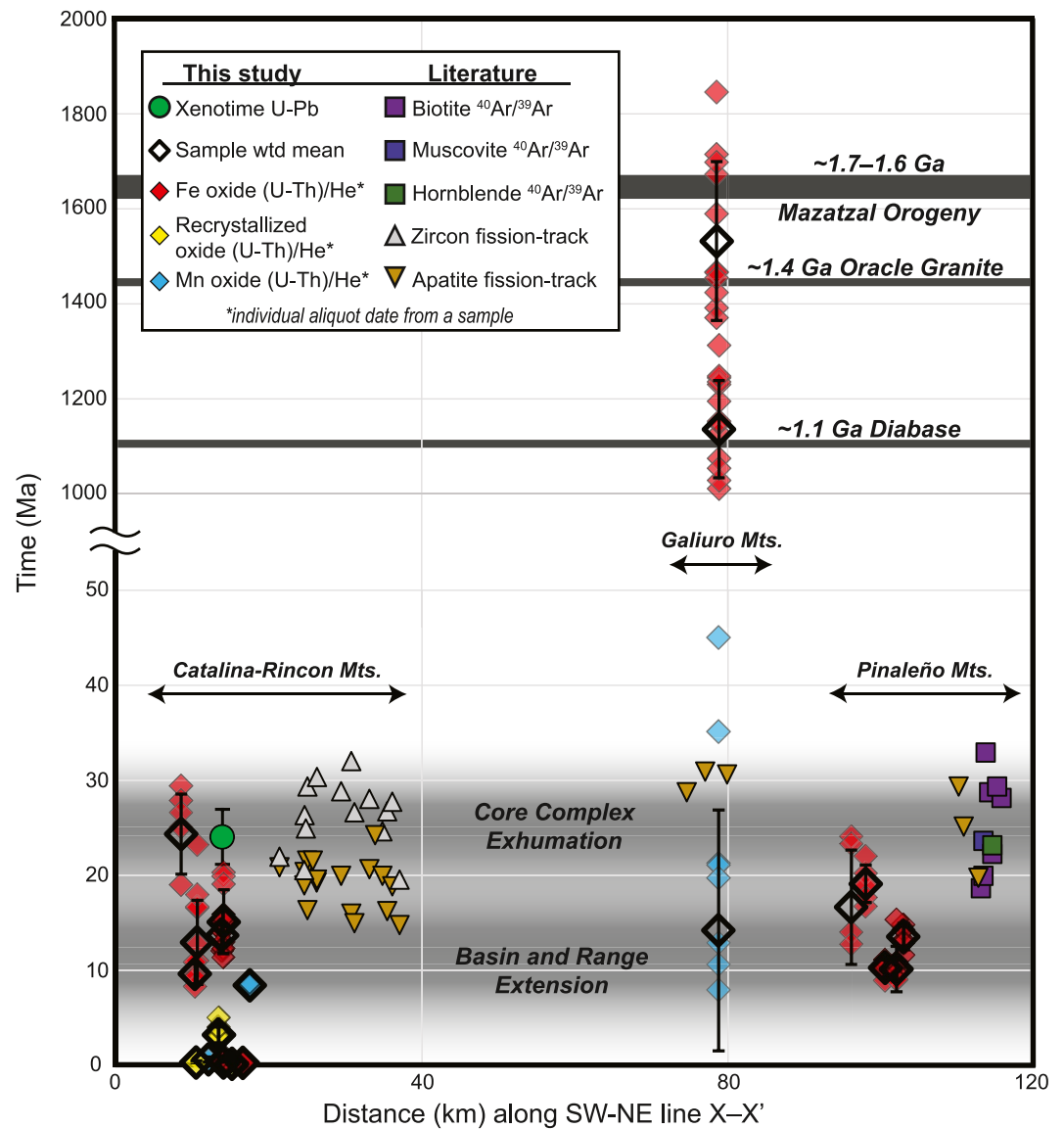


**Figure 7.** Sample dates plotted with respect to the extension-parallel transect. Error bars on oxide weighted means and compiled literature data are  $2\sigma$  analytical uncertainty. Apatite fission-track analyses come from Fayon et al. (2000) and Jepson et al. (2021), and biotite, muscovite, and hornblende  $^{40}\text{Ar}/^{39}\text{Ar}$  analyses are from Long et al. (1995). Color bars highlighting relevant magmatic/tectonic episodes were generated from literature ages (Anderson & Bender, 1989; Bickford et al., 2019; Bright et al., 2014; Copeland and Condie, 1986; Creasey et al., 1977; Fayon et al., 2000; Long et al., 1995; Meijer, 2014; Spencer et al., 1995; Stockli et al., 2002).

(for a total of four models) for only one sample, NEAC1C. In this case residuals were lower for Evenson kinetics. Residuals were significantly better (for both forward and inverse models) for sample NEAC1C than for NEAC3B or NEAC3C.

Using the  $D_0$  values proposed by the Farley (2018) and Evenson et al. (2014) studies we calculated apparent  $a$ , or diffusion domain length scale/size (domain radius for these models assuming spherical domain geometry). Relationships between apparent size and fraction of domains for all models are shown in Figure 6. Both hematite samples show positive correlations between domain fraction and apparent size. For example, in inverse models on NEAC1C, the largest apparent domain sizes for the Evenson and Farley kinetics contain 83% or 84%, respectively, of the  $^3\text{He}$ , and the second-largest domains contain 13.5% and 9.5%, respectively. For these same models, the two smallest domains for the Evenson and Farley kinetics models contain

only 3.5% and 6.5%, respectively (Table 3; Figure 6). These results are qualitatively consistent with the apparent crystal sizes observed in photomicrographs, in which most of the sample appears to be dominated by relatively large crystal sizes (Figures 2 and 6). More importantly, but not independently (because these models are based on the same step-heating results used to create the step-age plots), these results are also qualitatively consistent with fact that sample NEAC1C shows relatively young step ages for approximately 5%–10% of the  $^3\text{He}$  release (compared with the 3.5% and 6.5% of gas in apparently very small domains), but old apparent ages corresponding to the crystallization age of the rock for 90%–95% of the  $^3\text{He}$  release (Figure 5). The weighted bulk 10-°C/Ma-closure temperature for NEAC1C is 196–199 °C for the Evenson et al. (2014) kinetics, and 227–234 °C for the Farley (2018) kinetics.

The same relationships between apparent domain size and fraction also hold for the other hematite sample, NEAC3, based on both Evenson and Farley kinetics inverse models. In this case about 96% of the  $^3\text{He}$  appears to reside in two relatively large domains, and the remaining 4% in two much smaller domains (Table 3; Figure 6), again consistent with the step-age plots as well as qualitative appearance of the photomicrographs for this sample (Figure 2). The weighted bulk 10-°C/Ma-closure temperature for the inverse models on sample NEAC3B are 187 °C for the Evenson et al. (2014) kinetics, and 228 °C for the Farley (2018) kinetics.

In detail, the models reveal a significant difference between apparent domain sizes based on Farley (2018) or Evenson et al. (2014) kinetics. Specifically, predicted domain sizes are much larger for the Farley  $D_0$  than for the Evenson et al.  $D_0$ . For example, for the inverse models of sample NEAC1C, the domain with the largest fraction (83% or 84%) is predicted to be 90  $\mu\text{m}$  for the Evenson et al. kinetics, and 973  $\mu\text{m}$  for the Farley kinetics. Similarly, the domain with the second largest fraction (3.5%–9.5%) is predicted to be 3.5 versus 62  $\mu\text{m}$  for the same two kinetics, respectively. Similar contrasts exist for sample NEAC3B: the largest and most abundant domain for the Evenson et al. kinetics is 70 and 1,250  $\mu\text{m}$  for the Farley kinetics (for the second-largest domain, the sizes are 2.1 and 18  $\mu\text{m}$ , respectively). It is not straightforward to estimate actual dimensions of continuous single hematite crystals from photomicrographs for several reasons including the possibility of fine-scale crystal boundaries and fractures not visible at the scale of our observations (Figure 2). However, it seems likely that the approximate maximum diffusion domain size in an aliquot is not larger than the apparent size of the largest discernable continuous crystals. For hematite samples NEAC1C and NEAC3, the approximate dimensions of the largest crystals (either parallel or perpendicular to the elongated crystals) are probably tens, not hundreds or thousands, of  $\mu\text{m}$ . This may suggest that, if the length scales of the diffusion-domain size and crystallite size for hematite are indeed the same, the  $D_0$  of the Evenson et al. (2014) kinetics are more appropriate for at least these hematite samples.

On the other hand, at least at face value, for domains with small sizes and small fractions, the models using the Evenson et al. kinetics predict unrealistically small sizes for sample NEAC1C. For this sample, the predicted apparent length scales of the two smallest domains for the Evenson model are 0.1  $\mu\text{m}$  (4% of  $^3\text{He}$ ) and 0.1 nm (1%), whereas those for the Farley model are 7.7  $\mu\text{m}$  (3%) and 4.5  $\mu\text{m}$  (3.5%). The smallest of these, 0.1 nm, is roughly the size of a hematite unit cell. While it is not theoretically impossible that unit-cell sized domains control the release of  $\sim 1\%$  of the  $^3\text{He}$  in this sample, this seems unlikely. Importantly, however, models using *either* set of kinetics predict even smaller and more unrealistic sizes of 0.01–0.06 nm for the smallest domain (containing 1% of the  $^3\text{He}$ ). In all of these cases, use of either the Farley or Evenson models predict that domains with  $\sim 1\%$  of the  $^3\text{He}$  are unrealistically small. We suggest that rather than signifying volume diffusion over scales smaller than individual atoms, this points to some other factor besides  $E_a$ ,  $D_0$ , and domain size ( $a$ ) influencing the release and apparent kinetics of the earliest 1% of gas being released. Similar observations have also been made with He diffusion from zircon (e.g., Guenther et al., 2013; Reiners, 2005), for which the first few percent of He released is generally not considered for deriving diffusion kinetics for reasons that are not well understood but possibly related to minor crystal imperfections.

The forward model for Mn-oxide sample NEAC3T shows a very different relationship between domain size and fraction from that of the hematite. Domains with the largest fraction are also the smallest, and although the domain sizes span a similar or slightly larger range than those in hematite (four orders of magnitude, from 1 nm to 10  $\mu\text{m}$ ), they vary in fraction by only a factor of 3.5 (Table 3, Figure 6). The dominance of very small domain sizes is qualitatively consistent with the apparently extremely fine-grained appearance of the Mn-oxide (Figure 2), as well as with the continuous  $^4\text{He}/^3\text{He}$  step-age trend lacking any plateau. The

weighted bulk 10-°C/Ma-closure temperature for the Mn-oxide sample is 24°C (Table 3). This is similar to that determined from <sup>3</sup>He diffusion experiments on Mn-oxide with similar habit and appearance from another location (Garcia et al., 2018), which also yielded ages significantly younger than formation age, due to partial <sup>4</sup>He loss.

## 6.2. Interpretations of Regional (U-Th)/He Date Trends

The regional date trends of Fe- and Mn-oxides in faults and fractures (excluding those with young dates which we interpret as oxidized/recrystallized as discussed below) shows that shallowly exhumed normal-fault footwalls in the Galiuro Mountains yield Proterozoic dates from ca. 1.8 to 1.4 Ga and 1.3 to 1.0 Ga corresponding to magmatic events, specifically the eruption and emplacement of the rhyolite of the Pinal Schist and the intrusion of diabase dikes (Figures 3a and 7; Anderson & Bender, 1989; Anderson & Morrison, 2005; Bickford et al., 2019; Bright et al., 2014; Creasey & Krieger, 1978; Eisele & Isachsen, 2001; Shafiqullah et al., 1980). The hanging walls and deeply-exhumed footwalls of the Catalina-Rincon and Pinaleño-Jackson Mountain metamorphic core complexes at the southwest and northeast termini of this transect yield exclusively Oligocene and Miocene (U-Th)/He dates with increased population densities at ca. 24, 15, and 9 Ma overlapping in both regions (Figure 3b). Based on previous geo- and thermochronology studies, the distribution of dates from our oxide samples corresponds to known magmatic and tectonic events such as the exhumation of core complex footwalls, syn-extensional magmatic intrusions, and active periods of high-angle normal faulting during Basin and Range extension (Creasey et al., 1977; Davis et al., 2004; Ducea et al., 2020; Fayon et al., 2000; Jepson et al., 2021; Long et al., 1995; Shafiqullah et al., 1980; Terrien, 2012).

## 6.3. Proterozoic (U-Th)/He Dates From the Galiuro Mountains

(U-Th)/He dates of quartz/hematite vein sample NEAC1 from the Pinal Schist contains two groups of dates. The first group at ca. 1.7–1.6 Ga is consistent with the age of emplacement of its host rock, a metarhyolite composing the broader lithologic grouping of the Pinal Schist. The second group of dates from this sample are dispersed to younger dates of ca. 1.5–1.4 Ga. We speculate that partial post-formation He loss is causing these younger dates and may be due to (1) increased heat flow in the crust due to intrusions of the 1.4 Ga Oracle granite which was widely emplaced across southeastern Arizona (e.g., Anderson & Bender, 1989; Anderson & Morrison, 2005; Fornash et al., 2013) and/or (2) sedimentation and burial resulting in heating and increased He diffusion of relatively fine-grained aliquots prior to Cenozoic exhumation. Bulk closure temperature calculations of these samples suggest that heating due to nearby magmatism or sedimentation and burial would need to exceed ~175 °C (depending on the modeled kinetics and/or distribution of diffusion domain sizes) or approximately 6 km of burial depth (assuming an average geothermal gradient of 30 °C/km) to achieve partial resetting.

Aliquot date distributions of fracture-fill hematite sample NEAC3 from the Pinal Schist reflect a younger period of oxide formation at ca. 1.3–1.0 Ga associated with the intrusion of diabase dikes previously dated to 1.1 Ga in southeastern Arizona (including in Aravaipa Canyon and the Pinaleño Mountains) (Bright et al., 2014; Timmons et al., 2001). Based on the intercalation and close association of the hematite and Mn-oxide in sample NEAC3 and NEAC3T, we suggest that Mn-oxide sample NEAC3T likely formed at the same time as NEAC3, however, the very-fine grain-size of the Mn-oxide crystals resulted in low fractional He retention, leading to much younger dates, an interpretation supported by the <sup>3</sup>He diffusion data above (Figures 2, 5, and 6). At least part of the age variation observed among aliquots of NEAC3T is also likely due to mixing of small amounts of coarser-grained and more He-retentive hematite in some dated aliquots, an interpretation supported by a broad correlation between (U-Th)/He date and Fe and Mn concentrations among aliquots (Table S3 in Supporting Information S3).

## 6.4. Oligocene–Miocene (U-Th)/He Dates From Metamorphic Core Complexes

Fe- and Mn-oxide dates from the Catalina-Rincon and Pinaleño-Jackson Mountain core complexes record three periods of oxide formation and/or cooling associated with (1) core complex exhumation from ca. 30 to 20 Ma and syn-extensional magmatism ca. 27 to 25 Ma, and (2) remnant high heat flow and cooling of the

upper crust following core complex exhumation during Basin and Range extension and/or reactivation or introduction of new fluids to core complex-aged fractures during Basin and Range extension at ca. 15 and 9 Ma. Our initial expectations for date distributions of secondary oxides in the footwalls of the core complexes of southeastern Arizona were that we would find more samples with dates in the 30–20 Ma interval. Large detachment faults systems like those which exhumed the Catalina-Rincon and Pinaleno Mountains are hypothesized to carry significant fluids at elevated fluid pressures, and also include meteoric waters that penetrated fault and fracture zones, which could have been source-fluids for secondary oxides in core complex footwalls (Evenson et al., 2014; Kerrich & Rehrig, 1987; Reynolds & Lister, 1987). Syn-extensional magmatic events including the Catalina granite emplaced ca. 25 Ma in the Catalina Mountains, the eruption of the Galiuro Volcanics ca. 27 Ma in the Galiuro Mountains, and the Eagle Pass dike swarm at ca. 26 Ma in the Pinaleno Mountains likely exsolved magmatic fluids which also could have led to significant oxide precipitation, similar to what we observe from Proterozoic oxides related to magmatic events in the Galiuro Mountains (Creasey et al., 1977; Fornash et al., 2013; Keith et al., 1980; Nickerson, 2012). These magmatic events were followed by continued core complex exhumation throughout the region, generally interpreted to continue to ca. 20 Ma (Creasey et al., 1977; Fayon et al., 2000; Jepson et al., 2021; Keith et al., 1980; Long et al., 1995; Terrien, 2012). One might expect these events to have produced widespread hydrothermal circulation and precipitation of secondary oxides in faults and fractures in the uppermost few kilometers of the crust (e.g., Evenson et al., 2014; Morrison & Anderson, 1998; Spencer & Welty, 1986), however, only two samples in our study show dates in this interval: hematite from CH-3 (24 Ma), which is the only sample in our study from the hanging wall of a detachment fault, and xenotime from sample J107A (23 Ma), which is embedded in botryoidal hematite with dates of only 100 ka, both of which are from the Catalina-Rincon core complex (Figures 3b and 7).

One possible explanation for the paucity of 30–20 Ma dates of Fe- and Mn-oxides from core complex footwalls is that they record cooling dates resulting thermal relaxation following high heat flow in the crust long after core complex exhumation and during Basin and Range extension (Reiter, 2020; Sass et al., 1994). High heat flow in the crust could have kept samples with heterogeneous crystallite size distributions (fine-grained aliquots with low closure temperatures compared to coarse-grained aliquots with higher closure temperatures) in a partial retention zone yielding mixed-date populations like samples LWTV-01, LWTV-04, PH-1, and EP027 (Figures 3c, 3d and 7). Only two aliquots from the Pinaleno Mountains yield Oligocene (U-Th)/He dates while a majority of dates span the Miocene, which are significantly later than inferences of the timing of exhumation for the Pinaleno-Jackson Mountain core complex ca. 32–19 Ma from Long et al. (1995), and intrusions of syn-extensional dikes ca. 26 Ma (Nickerson, 2012; similar to estimates of exhumation of the Catalina-Rincon complex and intrusion of the Catalina granite). It is possible that many of the oxides present near 26 Ma dikes were deposited during the intrusions and they record cooling following magmatic activity and during exhumation along the Eagle Pass detachment fault. Slip along the Black Rock detachment fault (~15 km N of Eagle Pass) is estimated to have continued to ca. 19 Ma, and it is possible that the Eagle Pass detachment fault may have been active at the same time or potentially even later (Johnson & Loy, 1992; Kruger & Johnson, 1994; Long et al., 1995). Similar to the Catalina-Rincon samples, most Pinaleno oxides have dates of 16–14 Ma or 11–9 Ma which we interpret to likely represent cooling of magmatic/core complex exhumation-aged oxides with small diffusion domains and thus low closure temperatures.

Alternatively, if punctuated periods of high-angle normal faulting at ca. 15 and 9 Ma throughout the southern Basin and Range introduced new hydrothermal or meteoric fluids in pre-existing fault and fracture networks, partial resetting, oxidative recrystallization of original Fe- or Mn-oxides, and/or precipitation of new oxides may have taken place in these ancient features. In this scenario, Fe-oxides or sulfides precipitated in the initial core complex/magmatic episodes may have been metasomatically recrystallized either very recently, as in the case of the pseudomorphic cubic morphologies with very young (U-Th)/He dates (or where 23 Ma xenotime is surrounded by fine-grained 100 ka hematite), or during the Late-Miocene faulting/fluid circulation episodes that may have also precipitated new oxides at shallow depths, or reset pre-existing oxides. We speculate that if the earlier magmatic/exhumation episodes produced significant quantities of fault- and fracture-filling Fe-oxides, they were precipitated in the uppermost kilometer or so of the crust and eroded away, or they were recrystallized by later fluid flow. If correct, this could mean that in general, ages of fracture-hosted Fe-oxides near the surface today largely reflect the last major episode of circulation of oxidized fluids near the surface. Previous thermochronologic studies conducted throughout the Basin and Range province has also shown significant episodes of normal faulting and exhumation at 15 Ma and another

period at 9 Ma (e.g., Fosdick & Colgan, 2008; Spencer et al., 1995; Stockli et al., 2002) and we observe that recrystallization of oxides may be common in regions with multiple consecutive episodes of tectonism and faulting.

### 6.5. Pliocene and Younger Dates

Samples LWTV-03, LWTV-06, and LWTV-08 from Tanque Verde Ridge in the Catalina-Rincon metamorphic core complex represent the youngest date populations in the study ranging from 5 Ma to 6 ka (Figure 3c). These samples display petrographic and spectroscopic evidence of oxidative recrystallization including rusty, fine-grained hematite, cubic pseudomorphs of hematite after pyrite (or magnetite), sometimes accompanied by elevated concentrations of S. The original, relatively reduced Fe phases may have precipitated from fluids derived from core complex exhumation or Basin and Range faulting at greater depths in more reducing conditions. We suggest that these recrystallized or pseudomorphically replaced oxides with young dates reflect the timing of oxidation due to penetration of meteoric, oxidized fluids into fracture networks containing reduced phases leading to U uptake (e.g., Reiners et al., 2014) or He loss in pre-existing oxides and/or resetting of the (U-Th)/He system (e.g., Farley & McKeon, 2015). Farley and McKeon (2015) showed that most samples in their study yield ages of ca. 750 Ma, but one sample yields an age of ca. 450 Ma that they interpret as a recrystallization age, suggesting that Fe-oxide recrystallization may be a widespread process and should be accounted for when interpreting (U-Th)/He data. Considering recent to modern regional erosion rates in southern Arizona, the footwalls of these metamorphic core complexes may be eroding at approximately 0.05 km/Ma (e.g., Pelletier et al., 2013). If so, the approximately 1.0–0.1 Ma dates observed for most of these youngest samples would imply oxidation or recrystallization of sulfides or magnetite at depths of about 5–50 m depths. This predicts that reduced Fe minerals should be preserved and observed commonly in these regions at depths greater than ~50 m.

It is also possible that at least some of the microcrystalline samples that yield very young He dates may have been precipitated during Oligocene or Miocene time and have simply lost significant He since crystallization due to the low He retention properties of their microcrystalline hosts. Although we do not have diffusion-experiment data to support this, this is an alternative to the recrystallization hypothesis for these fine-grained samples, including 100-ka botryoidal hematite surrounding the 23 Ma xenotime in sample J107A. Samples J107A, J107B, and LWTV-02 exhibit fine-grain botryoidal or microcrystalline morphologies and all aliquots from these samples yield dates <1 Ma. This population of samples also yields a majority of aliquot dates ca. 100 ka. We also note, however, the one of the samples that yielded very young (<1 Ma) He dates, LWTV-08, from Tanque Verde Ridge in the Rincon Mountains, was not fine grained, and appeared more similar to specular hematite from other locations that yielded older ages. This supports a recrystallization origin, rather than primarily He-loss, for at least some of the young hematite dates observed in this study.

## 7. Conclusions

(U-Th)/He dates and He diffusion experiments on Fe- and Mn-oxides from southeastern Arizona show that secondary oxides in faults and fractures can be useful geochronometers to estimate the timing of formation associated with tectonic or magmatic/hydrothermal events. Such interpretations are most straightforward for relatively coarse-grained specular hematite. In contrast, fine-grained Fe- and Mn-oxides display much younger dates likely associated with either recrystallization or pseudomorphic replacement, or loss of large fractions of radiogenic He. Oxide date distributions across southeastern Arizona are consistent with periods of tectonic, magmatic, and hydrothermal activity from the Proterozoic to the Cenozoic. He diffusion experiments on several samples highlight the effects of diffusion-domain size on <sup>4</sup>He retention of polycrystalline aggregates and bulk closure temperature. To first order, poly-domain diffusion modeling points to distributions of domain sizes and fractions qualitatively consistent with crystal size distributions within samples. Samples with greater proportions of large diffusion-domain sizes indicate greater He retentivity and yield bulk closure temperatures higher than finer-grain morphologies. However, significant differences in modeled domain sizes (and closure temperatures) result from the use of different kinetic models.

(U-Th)/He dates of Fe-oxides from the Galiuro Mountains are consistent with Proterozoic magmatic events at ca. 1.7–1.6 Ga and 1.1 Ga. (U-Th)/He dates from the Catalina-Rincon and Pinaléño metamorphic core complexes are consistent with the timing of two distinct extensional styles; core complex exhumation from ca. 30–20 Ma and/or magmatic intrusions ca. 27–25 Ma, followed by Basin and Range extension from 20 to 5 Ma, with date populations clustered at ca. 15 and 9 Ma. The most recent period of oxide mineralization from detachment fault zones and fractures with dates mostly <1 Ma are likely caused by oxidative recrystallization or pseudomorphic replacement that reset the (U-Th)/He system yielding oxidation dates instead of cooling or crystallization ages of the original oxide/sulfide. However, because many of these samples also have a relatively fine-grained botryoidal habit, we cannot rule out low He retentivity from sub-micron diffusion domains as the origin of at least some of these samples. Petrographic investigations of oxide textures and morphologies indicate that apparent crystallite size and morphology have first order controls on (U-Th)/He dates. Correlations between apparent crystal sizes and textures with (U-Th)/He dates indicates that in-depth qualitative and quantitative petrographic and spectroscopic investigations of Fe- and Mn-oxides are helpful for interpreting oxide (U-Th)/He thermochronology data.

### Data Availability Statement

The data presented in this publication are available at EarthChem (<https://doi.org/10.26022/IEDA/112074>).

### Acknowledgments

We acknowledge analytical assistance from Uttam Chowdhury, Ken Domanik, Kojo Plange, Lydia Bailey, and Mark Pecha. We thank Jon Pelletier for LiDAR images of Tanque Verde Ridge, Chris Clinkscapes for help with sample collection, and helpful discussion from Jay Chapman and Simone Runyon. We thank the Rincon Mountain District of the Saguaro National Park Service for allowing field access and sample collection. This work was supported by NSF grant EAR 1219653 to PWR. SHS acknowledges additional funding from the University of Wyoming Department of Geology and Geophysics. We thank Peter van der Beek for editorial handling and Dr. Florian Hofmann and two anonymous reviewers whose comments greatly improved this manuscript.

### References

- Anderson, J. L., Barth, A. P., & Young, E. D. (1988). Mid-crustal Cretaceous roots of Cordilleran metamorphic core complexes. *Geology*, *16*(4), 366–369. [https://doi.org/10.1130/0091-7613\(1988\)016<0366:MCCROC>2.3.CO;2](https://doi.org/10.1130/0091-7613(1988)016<0366:MCCROC>2.3.CO;2)
- Anderson, J. L., & Bender, E. E. (1989). Nature and origin of Proterozoic A-type granitic magmatism in the southwestern United States of America. *Lithosphere*, *23*(1–2), 19–52. [https://doi.org/10.1016/0024-4937\(89\)90021-2](https://doi.org/10.1016/0024-4937(89)90021-2)
- Anderson, J. L., & Morrison, J. (2005). Ilmenite, magnetite, and peraluminous Mesoproterozoic anorogenic granites of Laurentia and Baltica. *Lithos*, *80*(1–4), 45–60. <https://doi.org/10.1016/j.lithos.2004.05.008>
- Arca, M. S., Kapp, P., & Johnson, R. A. (2010). Cenozoic crustal extension in southeastern Arizona and implications for models of core-complex development. *Tectonophysics*, *488*, 174–190. <https://doi.org/10.1016/j.tecto.2010.03.021>
- Ault, A. K., Frenzel, M., Reiners, P. W., Woodcock, N. H., & Thomson, S. N. (2016). Record of paleofluid circulation in faults revealed by hematite (U-Th)/He and apatite fission-track dating: An example from Gower Peninsula fault fissures, Wales. *Lithosphere*, *8*(4), 379–385. <https://doi.org/10.1130/L522.1>
- Ault, A. K., Reiners, P. W., Evans, J. P., & Thomson, S. N. (2015). Linking hematite (U-Th)/He dating with the microtextural record of seismicity in the Wasatch fault damage zone, Utah, USA. *Geology*, *43*(9), 771–774. <https://doi.org/10.1130/G36897.1>
- Bähr, R., Lippolt, H. J., & Wernicke, R. S. (1994). Temperature-induced <sup>4</sup>He degassing of specularite and botryoidal hematite: A <sup>4</sup>He retentivity study. *Journal of Geophysical Research*, *99*(B9), 17695–17707. <https://doi.org/10.1029/94jb01055>
- Bickford, M. E., Mueller, P. A., Condie, K. C., Hanan, B. B., & Kamenov, G. D. (2019). Ages and Hf isotopic compositions of detrital zircons in the Pinal schist, southern Arizona, USA: Provenance, tectonic setting, and evidence for pre-1.7 Ga crust in SW Laurentia. *Precambrian Research*, *331*, 105374. <https://doi.org/10.1016/j.precamres.2019.105374>
- Bright, R. M., Amato, J. M., Denyszyn, S. W., & Ernst, R. E. (2014). U-Pb geochronology of 1.1 Ga diabase in the southwestern United States: Testing models for the origin of a post-Grenville large igneous province. *Lithosphere*, *6*(3), 135–156. <https://doi.org/10.1130/L335.1>
- Calzolari, G., Rossetti, F., Ault, A. K., Lucci, F., Olivetti, V., & Nozaem, R. (2018). Hematite (U-Th)/He thermochronometry constrains intraplate strike-slip faulting on the Kuh-e-Faghan Fault, central Iran. *Tectonophysics*, *728*, 41–54. <https://doi.org/10.1016/j.tecto.2018.01.023>
- Cecil, M. R., Gehrels, G., Ducea, M. N., & Patchett, P. J. (2011). U-Pb-Hf characterization of the central Coast Mountains batholith: Implications for petrogenesis and crustal architecture. *Lithosphere*, *3*(4), 247–260. <https://doi.org/10.1130/L134.1>
- Condie, K. C., & DeMalas, J. P. (1985). The Pinal Schist: An early Proterozoic quartz wacke association in southeastern Arizona. *Precambrian Research*, *27*(4), 337–356. [https://doi.org/10.1016/0301-9268\(85\)90093-2](https://doi.org/10.1016/0301-9268(85)90093-2)
- Copeland, P., & Condie, K. C. (1986). Geochemistry and tectonic setting of lower Proterozoic supracrustal rocks of the Pinal Schist, southeastern Arizona. *The Geological Society of America Bulletin*, *97*(12), 1512–1520. [https://doi.org/10.1130/0016-7606\(1986\)97<1512:gatsol>2.0.co;2](https://doi.org/10.1130/0016-7606(1986)97<1512:gatsol>2.0.co;2)
- Creasey, S. C., Banks, N. G., Ashley, R. P., & Theodore, T. G. (1977). Middle Tertiary plutonism in the Santa Catalina and Tortolita Mountains, Arizona. *Journal of Research of the US Geological Survey*, *5*, 705–717.
- Creasey, S. C., & Krieger, M. H. (1978). Galiuro Volcanics, Pinal, Graham and Cochise counties, Arizona. *Journal of Research of the U. S. Geological Survey*, *6*, 115–131.
- Davis, G. H., Constenius, K. N., Dickinson, W. R., Rodríguez, E. P., & Cox, L. J. (2004). Fault and fault-rock characteristics associated with Cenozoic extension and core-complex evolution in the Catalina-Rincon region, southeastern Arizona. *The Geological Society of America Bulletin*, *116*(1–2), 128–141. <https://doi.org/10.1130/B25260.1>
- Davis, G. H., & Hardy, J. (1981). The Eagle Pass detachment, southeastern Arizona: Product of mid-Miocene listric (?) normal faulting in the southern Basin and Range. *Geological Society of America Bulletin*, *92*(10), 749–762. [https://doi.org/10.1130/0016-7606\(1981\)92<749:tepsa>2.0.co;2](https://doi.org/10.1130/0016-7606(1981)92<749:tepsa>2.0.co;2)
- Dickinson, W. R. (1991). *Tectonic Setting of Faulted Tertiary Strata Associated with the Catalina Core Complex in Southern Arizona* (Vol. 264, pp. 1–106). Geological Society of America. <https://doi.org/10.1130/SPE264-p1>
- Ducea, M. N., Triantafyllou, A., & Krcmaric, J. (2020). New timing and depth constraints for the Catalina metamorphic core complex, Southeast Arizona. *Tectonics*, *39*(8), e2020TC006383. <https://doi.org/10.1029/2020TC006383>

- Eisele, J., & Isachsen, C. E. (2001). Crustal growth in southern Arizona: U-Pb geochronologic and Sm-Nd isotopic evidence for addition of the Paleoproterozoic Cochise block to the Mazatzal province. *American Journal of Science*, 301(9), 773–797. <https://doi.org/10.2475/ajs.301.9.773>
- Evenson, N. S., Reiners, P. W., Spencer, J. E., & Shuster, D. L. (2014). Hematite and Mn oxide (U-Th)/He dates from the Buckskin-Rawhide detachment system, western Arizona: Gaining insights into hematite (U-Th)/He systematics. *American Journal of Science*, 314(10), 1373–1435. <https://doi.org/10.2475/10.2014.01>
- Farley, K. A. (2018). Helium diffusion parameters of hematite from a single-diffusion-domain crystal. *Geochimica et Cosmochimica Acta*, 231, 117–129. <https://doi.org/10.1016/j.gca.2018.04.005>
- Farley, K. A., & Flowers, R. M. (2012). (U-Th)/Ne and multidomain (U-Th)/He systematics of a hydrothermal hematite from eastern Grand Canyon. *Earth and Planetary Science Letters*, 359, 131–140. <https://doi.org/10.1016/j.epsl.2012.10.010>
- Farley, K. A., & McKeon, R. (2015). Radiometric dating and temperature history of banded iron formation-associated hematite, Gogebic iron range, Michigan, USA. *Geology*, 43(12), 1083–1086. <https://doi.org/10.1130/G37190.1>
- Favorito, D. A., & Seedorff, E. (2018). Discovery of major basement-cored uplifts in the northern Galiuro Mountains, Southeastern Arizona: Implications for regional Laramide deformation style and structural evolution. *Tectonics*, 37(10), 3916–3940. <https://doi.org/10.1029/2018TC005180>
- Fayon, A. K., Peacock, S. M., Stump, E., & Reynolds, S. J. (2000). Fission track analysis of the footwall of the Catalina detachment fault, Arizona: Tectonic denudation, magmatism, and erosion. *Journal of Geophysical Research*, 105(B5), 11047–11062. <https://doi.org/10.1029/1999JB900421>
- Fornash, K. F., Patchett, P. J., Gehrels, G. E., & Spencer, J. E. (2013). Evolution of granitoids in the Catalina metamorphic core complex, southeastern Arizona: U-Pb, Nd, and Hf isotopic constraints. *Contributions to Mineralogy and Petrology*, 165(6), 1295–1310. <https://doi.org/10.1007/s00410-013-0859-4>
- Fosdick, J. C., & Colgan, J. P. (2008). Miocene extension in the East Range, Nevada: A two-stage history of normal faulting in the northern basin and range. *Geological Society of America Bulletin*, 120(9–10), 1198–1213. <https://doi.org/10.1130/B26201.1>
- Garcia, V. H., Reiners, P. W., Shuster, D. L., Idleman, B., & Zeitler, P. K. (2018). Thermochronology of sandstone-hosted secondary Fe- and Mn-oxides near Moab, Utah: Record of paleo-fluid flow along a fault. *GSA Bulletin*, 130(1–2), 93–113. <https://doi.org/10.1130/B31627.1>
- Gehrels, G. E., & Pecha, M. (2014). Detrital zircon U-Pb geochronology and Hf isotope geochemistry of Paleozoic and Triassic passive margin strata of western North America. *Geosphere*, 10(1), 49–65.
- Gehrels, G. E., Valencia, V. A., & Ruiz, J. (2008). Enhanced precision, accuracy, efficiency, and spatial resolution of U-Pb ages by laser ablation-multicollector-inductively coupled plasma-mass spectrometry. *Geochemistry, Geophysics, Geosystems*, 9(3), a-n. <https://doi.org/10.1029/2007GC001805>
- Ginster, U., & Reiners, P. W. (2018). Error propagation in the derivation of noble gas diffusion parameters for minerals from step heating experiments. *Geochemistry, Geophysics, Geosystems*, 19(10), 3706–3720. <https://doi.org/10.1029/2018GC007531>
- Guenther, W. R., Reiners, P. W., Ketcham, R. A., Nasdala, L., & Giester, G. (2013). Helium diffusion in natural zircon: Radiation damage, anisotropy, and the interpretation of zircon (U-Th)/He thermochronology. *American Journal of Science*, 313(3), 145–198. <https://doi.org/10.2475/03.2013.01>
- Hofmann, F., Treffkorn, J., & Farley, K. A. (2020). U-loss associated with laser-heating of hematite and goethite in vacuum during (U-Th)/He dating and prevention using high O<sub>2</sub> partial pressure. *Chemical Geology*, 532, 119350. <https://doi.org/10.1016/j.chemgeo.2019.119350>
- Jensen, J. L., Siddoway, C. S., Reiners, P. W., Ault, A. K., Thomson, S. N., & Steele-MacInnis, M. (2018). Single-crystal hematite (U-Th)/He dates and fluid inclusions document widespread Cryogenian sand injection in crystalline basement. *Earth and Planetary Science Letters*, 500, 145–155. <https://doi.org/10.1016/j.epsl.2018.08.021>
- Jepson, G., Carrapa, B., George, S. W., Triantafyllou, A., Egan, S. M., Constenius, K. N., et al. (2021). Resolving mid-to upper-crustal exhumation through apatite petrochronology and thermochronology. *Chemical Geology*, 565, 120071. <https://doi.org/10.1016/j.chemgeo.2021.120071>
- Johnson, R. A., & Loy, K. L. (1992). Seismic reflection evidence for seismogenic low-angle faulting in southeastern Arizona. *Geology*, 20(7), 597–600. [https://doi.org/10.1130/0091-7613\(1992\)020<0597:srefsl>2.3.co;2](https://doi.org/10.1130/0091-7613(1992)020<0597:srefsl>2.3.co;2)
- Keep, M. (1996). The Pinal Schist, southeast Arizona, USA: Contraction of a Palaeoproterozoic rift basin. *Journal of the Geological Society*, 153(6), 979–993. <https://doi.org/10.1144/gsjgs.153.6.0979>
- Keith, S. B., Reynolds, S., Damon, P. E., Shafiqullah, M., Livingston, D. E., & Pushkar, P. D. (1980). Evidence for multiple intrusion and deformation within the Santa Catalina-Rincon-Tortolita crystalline complex. *Southeastern Arizona* (Vol. 153, pp. 217–267). Memoir of the Geological Society of America. <https://doi.org/10.1130/MEM153-p217>
- Kerrick, R., & Rehrig, W. (1987). Fluid motion associated with Tertiary mylonitization and detachment faulting: <sup>18</sup>O/<sup>16</sup>O evidence from the Pí-cacho metamorphic core complex, Arizona. *Geology*, 15(1), 58–62. [https://doi.org/10.1130/0091-7613\(1987\)15<58:fmawtm>2.0.co;2](https://doi.org/10.1130/0091-7613(1987)15<58:fmawtm>2.0.co;2)
- Krieger, M. H. (1968). *Ash-flow tuffs in the northern Galiuro Mountains, County, Arizona* [Abstract]. In *Abstr. for 1968*. Geological Society of America Special Paper 121:523.
- Krieger, M. H. (1974). *Geologic map of the Black Mountain quadrangle, Pinal County, Arizona* (p. 4). US Geological Survey.
- Kruger, J. M., & Johnson, R. A. (1994). Raft model of crustal extension: Evidence from seismic reflection data in southeast Arizona. *Geology*, 22(4), 351–354. [https://doi.org/10.1130/0091-7613\(1994\)022<0351:rmocee>2.3.co;2](https://doi.org/10.1130/0091-7613(1994)022<0351:rmocee>2.3.co;2)
- Lippolt, H. J., & Hautmann, S. (1995). <sup>40</sup>Ar/<sup>39</sup>Ar ages of Precambrian manganese ore minerals from Sweden, India and Morocco. *Mineralium Deposita*, 30(3), 246–256. <https://doi.org/10.1007/BF00196360>
- Lippolt, H. J., Wernicke, R. S., & Boschmann, W. (1993). <sup>4</sup>He diffusion in specular hematite. *Physics and Chemistry of Minerals*, 20(6), 415–418. <https://doi.org/10.1007/bf00203111>
- Long, K. B., Gehrels, G. E., & Baldwin, S. L. (1995). Tectonothermal evolution of the Pinaleno-Jackson Mountain core complex, southeast Arizona. *Geological Society of America Bulletin*, 107(10), 1231–1240. [https://doi.org/10.1130/0016-7606\(1995\)107<1231:teotpo>2.3.co;2](https://doi.org/10.1130/0016-7606(1995)107<1231:teotpo>2.3.co;2)
- Lovera, O. M., Richter, F. M., & Harrison, T. M. (1991). Diffusion domains determined by <sup>39</sup>Ar released during step heating. *Journal of Geophysical Research*, 96(B2), 2057–2069. <https://doi.org/10.1029/90jb02217>
- Meijer, A. (2014). The Pinal Schist of southern Arizona: A Paleoproterozoic forearc complex with evidence of spreading ridge-trench interaction at ca. 1.65 Ga and a Proterozoic arc obduction event. *GSA Bulletin*, 126(9–10), 1145–1163. <https://doi.org/10.1130/B31002.1>
- Morrison, J., & Anderson, J. L. (1998). Footwall refrigeration along a detachment fault: Implications for the thermal evolution of core complexes. *Science*, 279(5347), 63–66. <https://doi.org/10.1126/science.279.5347.63>
- Moser, A. C., Evans, J. P., Ault, A. K., Janecke, S. U., & Bradbury, K. K. (2017). (U-Th)/He thermochronometry reveals Pleistocene punctuated deformation and synkinematic hematite mineralization in the Mecca Hills, southernmost San Andreas Fault zone. *Earth and Planetary Science Letters*, 476, 87–99. <https://doi.org/10.1016/j.epsl.2017.07.039>
- Nickerson, P. A. (2012). *Post-mineral normal faulting in Arizona porphyry systems (Ph.D. thesis)* (p. 310). University of Arizona.

- Pelletier, J. D., Barron-Gafford, G. A., Breshears, D. D., Brooks, P. D., Chorover, J., Durcik, M., et al. (2013). Coevolution of nonlinear trends in vegetation, soils, and topography with elevation and slope aspect: A case study in the sky islands of southern Arizona. *Journal of Geophysical Research: Earth Surface*, *118*(2), 741–758. <https://doi.org/10.1002/jgrf.20046>
- Reiners, P. W. (2005). Zircon (U-Th)/He thermochronometry. *Reviews in Mineralogy and Geochemistry*, *58*(1), 151–179. <https://doi.org/10.2138/rmg.2005.58.6>
- Reiners, P. W., Chan, M. A., & Evenson, N. S. (2014). (U-Th)/He geochronology and chemical compositions of diagenetic cement, concretions, and fracture-filling oxide minerals in Mesozoic sandstones of the Colorado Plateau. *GSA Bulletin*, *126*(9–10), 1363–1383. <https://doi.org/10.1130/B30983.1>
- Reiter, M. (2020). Heat flow data in an area of the eastern southern basin and range in Arizona contribute to an analysis of neogene lithosphere thinning greater than 100 km. *Lithosphere*, *2020*(1), 8872618. <https://doi.org/10.2113/2020/8872618>
- Reynolds, S. J., & Lister, G. S. (1987). Structural aspects of fluid-rock interactions in detachment zones. *Geology*, *15*(4), 362–366. [https://doi.org/10.1130/0091-7613\(1987\)15<362:saofii>2.0.co;2](https://doi.org/10.1130/0091-7613(1987)15<362:saofii>2.0.co;2)
- Sass, J. H., Lachenbruch, A. H., Galanis, S. P., Jr, Morgan, P., Priest, S. S., Moses, T. H., Jr, & Munroe, R. J. (1994). Thermal regime of the southern Basin and Range Province: 1. Heat flow data from Arizona and the Mojave Desert of California and Nevada. *Journal of Geophysical Research*, *99*(B11), 22093–22119. <https://doi.org/10.1029/94JB01891>
- Shafiqullah, M., Damon, P. E., Lynch, D. J., Reynolds, S. J., Rehrig, W. A., & Raymond, R. H. (1980). K-Ar geochronology and geologic history of southwestern Arizona and adjacent areas. *Arizona Geological Society Digest*, *12*, 201–260.
- Shuster, D. L., Farley, K. A., Sistierson, J. M., & Burnett, D. S. (2004). Quantifying the diffusion kinetics and spatial distributions of radiogenic <sup>4</sup>He in minerals containing proton-induced <sup>3</sup>He. *Earth and Planetary Science Letters*, *217*(1–2), 19–32. [https://doi.org/10.1016/S0012-821X\(03\)00594-6](https://doi.org/10.1016/S0012-821X(03)00594-6)
- Shuster, D. L., Vasconcelos, P. M., Heim, J. A., & Farley, K. A. (2005). Weathering geochronology by (U-Th)/He dating of goethite. *Geochimica et Cosmochimica Acta*, *69*(3), 659–673. <https://doi.org/10.1016/j.gca.2004.07.028>
- Spencer, J. E., Richard, S. M., Reynolds, S. J., Miller, R. J., Shafiqullah, M., Gilbert, W. G., & Grubensky, M. J. (1995). Spatial and temporal relationships between mid-Tertiary magmatism and extension in southwestern Arizona. *Journal of Geophysical Research*, *100*(B6), 10321–10351. <https://doi.org/10.1029/94JB02817>
- Spencer, J. E., & Welty, J. W. (1986). Possible controls of base- and precious-metal mineralization associated with tertiary detachment faults in the lower Colorado River trough, Arizona and California. *Geology*, *14*(3), 195–198. [https://doi.org/10.1130/0091-7613\(1986\)14<195:pcobap>2.0.co;2](https://doi.org/10.1130/0091-7613(1986)14<195:pcobap>2.0.co;2)
- Stockli, D. F., Surpless, B. E., Dumitru, T. A., & Farley, K. A. (2002). Thermochronological constraints on the timing and magnitude of Miocene and Pliocene extension in the central Wassuk Range, western Nevada. *Tectonics*, *21*(4), 10–11. <https://doi.org/10.1029/2001TC001295>
- Terrien, J. (2012). *The role of magmatism in the Catalina metamorphic core complex, Arizona: Insights from integrated thermochronology, gravity and aeromagnetic data (Ph.D. thesis)*. University of Arizona.
- Thorman, C. H., & Naruk, S. J. (1987). *Generalized bedrock geologic map and distribution of mylonitic rocks in the eastern Pinaleno Mountains*. Graham County, Arizona.
- Timmons, J. M., Karlstrom, K. E., Dehler, C. M., Geissman, J. W., & Heizler, M. T. (2001). Proterozoic multistage (ca. 1.1 and 0.8 Ga) extension recorded in the Grand Canyon Supergroup and establishment of northwest- and north-trending tectonic grains in the southwestern United States. *GSA Bulletin*, *113*(2), 163–181. [https://doi.org/10.1130/0016-7606\(2001\)113<0163:pmcage>2.0.co;2](https://doi.org/10.1130/0016-7606(2001)113<0163:pmcage>2.0.co;2)
- Tremblay, M. M., Shuster, D. L., & Balco, G. (2014). Diffusion kinetics of <sup>3</sup>He and <sup>21</sup>Ne in quartz and implications for cosmogenic noble gas paleothermometry. *Geochimica et Cosmochimica Acta*, *142*, 186–204. <https://doi.org/10.1016/j.gca.2014.08.010>
- Wernicke, R. S., & Lippolt, H. J. (1993). Botryoidal hematite from the Schwarzwald (Germany): Heterogeneous uranium distributions and their bearing on the helium dating method. *Earth and Planetary Science Letters*, *114*(2–3), 287–300. [https://doi.org/10.1016/0012-821X\(93\)90031-4](https://doi.org/10.1016/0012-821X(93)90031-4)
- Wernicke, R. S., & Lippolt, H. J. (1994). Dating of vein specularite using internal (U+Th)/<sup>4</sup>He isochrons. *Geophysical Research Letters*, *21*(5), 345–347. <https://doi.org/10.1029/94GL00014>